Dissipation in Frequency Selective Structures

Widenberg, Björn

2002

CODEN:LUTEDX/(TEAT-7107)/1-31/(2002)

Dissipation in Frequency Selective Structures

Björn Widenberg

Department of Electroscience
Electromagnetic Theory
Lund Institute of Technology
Sweden

Björn Widenberg

Department of Electroscience
Electromagnetic Theory
Lund Institute of Technology
P.O. Box 118
SE-221 00 Lund
Sweden

Editor: Gerhard Kristensson

Abstract

Dissipation in Frequency Selective Structures (FSS) of aperture/slot type is studied. The FSS consists of an arbitrary number of aperture layers and dielectric layers. An aperture layer consists of a conducting plate with a periodic array of apertures, with arbitrary cross-section. The dissipation in an FSS is due to losses in the dielectric material, and losses due to finite conductivity in the metallic plate. The dissipation in the dielectric parts is modelled by the complex permittivity. The dissipation on the metallic structure arises both on the plane metallic surface and on the metallic walls of the apertures.

The method used to analyze the FSS is based on the mode matching technique and the Finite Element Method (FEM). The apertures are treated as waveguides. The field are expanded in Floquet modes and waveguide modes, and scattering matrices are derived. The attenuation and the power losses are calculated for a number of different FSS, and based on these results the performance of an FSS with losses is discussed.

1 Introduction

In this paper the dissipation of power in Frequency Selective Structures (FSS) of aperture/slot type is studied by a mode matching technique. FSS are most often constructed from one or more metallic screens that are sandwiched between dielectric slabs, see Figure 1. The metallic screens are perforated in a regular pattern such that at the resonant frequency of the structure, the radome passes nearly 100% of the incident power. Outside the passband, nearly all of the incident power is reflected. In essence, these radomes provide a bandpass filter function to the antennas located behind them. Extensive discussions on FSS can be found in [8, 11, 14].

The dissipation in an FSS is due to losses in the dielectric material, and losses due to the finite conductivity in the metallic plate. The dissipation in the dielectric parts is taken into account by the complex permittivity. The dissipation on the metallic plate arises both on the plane metallic surface and on the metallic walls of the apertures, and is modelled by the introduction of a surface resistance.

Lossless cascaded FSS have been treated in a number of papers. In [10] a multilayered interface with each layer comprising metal strips periodically mounted on lossy dielectric substrate is examined. An arbitrary screen that consists of periodic metallic surfaces which are cascaded with lossy dielectric layers is analyzed in [4, 5]. In [7] a lossy structure, composed of a thin crossed-slot aperture backed by a lossy dielectric layer, has been considered. A numerical method for lossy FSS in the millimeter-wave range has been carried out in [9]. In [1] infinite rectangular grids with finite conductivity are analyzed. Waveguides filled with lossy medium and with lossy walls are studied among others in [2].

The presence of dissipation in the dielectric medium and the metallic surfaces in an FSS modifies the usual description of scattering by an FSS. This modification takes the form of a complex rather than a real propagation constant (k_z or γ). The complex propagation constant may be expressed as $k_z = \beta + i\alpha$. The phase

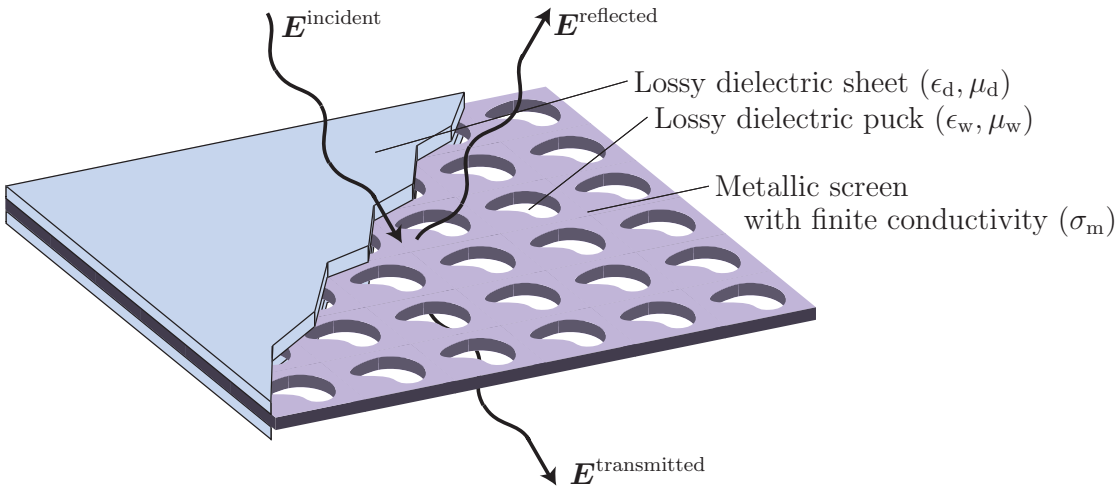

Figure 1: A Frequency Selective Structure (FSS).

constant, $\beta = 2\pi/\lambda$, and the attenuation constant, α, are determined by the type of dissipation, the type of material, the mode in question, and the geometry of the FSS. The quantity $20\log_{10}(\mathrm{e}^{\alpha}) \approx 8.686\alpha$, the decibels of attenuation per unit length is frequently employed as a measure of attenuation instead of α.

In the next section the geometry for the FSS and the mode matching technique are described. The scattering matrix and the calculation of the internal fields are discussed in Section 3. Section 4 is devoted to the transmitted power flow, and the flow is illustrated in several plots. The losses in the dielectric regions are described in Section 5, where a number of different FSS with dissipation are investigated. In Section 6 some surface fields are depicted, and the losses in the plane metallic screen are discussed. Finally waveguides with lossy walls are analyzed in Section 7. Numerical values of dissipation in the plane metallic screen and in the metallic walls for some FSS are presented. In the concluding remarks in Section 8 the importance of dissipation is discussed.

2 Geometry and method

The geometry of a simple FSS, that consists of a perforated conducting plate sandwiched between two dielectric slabs, is depicted in Figure 1. The screen can have an arbitrary number of aperture layers and dielectric layers. An aperture layer consists of an electrically conducting plate perforated with a periodic array of apertures. The apertures can have arbitrary cross-section, and every element in the aperture layer is assumed to be a waveguide element. The apertures can be filled with a dielectric material and any number of dielectric layers is allowed on either side of the conductive screen. In Figure 2 the cross-section of the simple FSS in Figure 1 is depicted.

The grid for the periodic structure is defined in Figure 3, where it is assumed

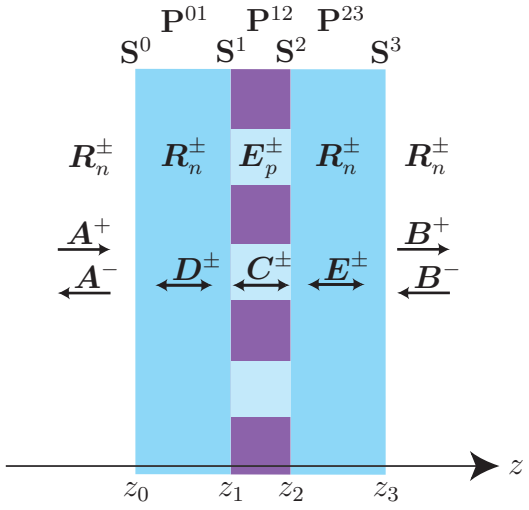

Figure 2: A cross-section of an FSS, with the expansion modes $\boldsymbol{R}_n^{\pm}$, $\boldsymbol{E}_p^{\pm}$, the mode coefficients $\boldsymbol{A}^{\pm}$, $\boldsymbol{B}^{\pm}$, $\boldsymbol{C}^{\pm}$, $\boldsymbol{D}^{\pm}$, $\boldsymbol{E}^{\pm}$, the scattering matrices $\mathbf{S}^0$, $\mathbf{S}^1$, $\mathbf{S}^2$, $\mathbf{S}^3$, and propagation matrices $\mathbf{P}^{01}$, $\mathbf{P}^{12}$, $\mathbf{P}^{23}$.

that the structure is infinite in the xy-plane. The z-axis is assumed to be orthogonal to the surface of the conducting screen. The apertures are spaced periodically along the x-axis with period a. The other axis of periodicity y' makes an angle ϕ_0 with the x-axis and the apertures are spaced periodically along this second axis with period b, see Figure 3. Hence, the array of apertures is divided into identical cells. The cell at the origin is called the unit cell, and is denoted $D \in \mathbb{R}^2$. The cross-section of the aperture at the unit cell is denoted $\Omega \in \mathbb{R}^2$, $\Omega \subset D$.

The method for analyzing the FSS is based on a general mode-matching technique and cascade coupling [12]. The FSS is divided into a number of boundaries and uniform layers, see Figure 2, and the fields in each layer are expanded in a complete set of vector wave functions. The mode matching technique is based on the matching of the tangential electric and magnetic fields at each junction between uniform sections.

The tangential electric and magnetic fields outside the screen and inside the dielectric layers, see Figure 2, are expanded in Floquet modes, $\boldsymbol{R}_{\mathrm{T}ln}$ and $\boldsymbol{T}_{\mathrm{T}ln}$, see *e.g.*, [11–13]. The Floquet modes form a complete and orthonormal set of tangential plane waves. The tangential fields inside the aperture layers, see Figure 2, are expanded in waveguide modes, $\boldsymbol{E}_{\mathrm{T}p}$ and $\boldsymbol{H}_{\mathrm{T}p}$, see *e.g.*, [2]. The sets of waveguide modes are complete and orthogonal. The geometry of the aperture is arbitrary. This is possible since the method does not rely on explicit expressions for the waveguide modes. Instead the Finite Element Method (FEM) is used to obtain the appropriate modes.

The tangential electric and magnetic fields are matched by the boundary conditions at every boundary surface between uniform section of the structure, in order to obtain a scattering matrix $\mathbf{S}^n$, see Figure 2. Each junction along the FSS has its own scattering matrix and the scattering matrix represents the scattering prop-

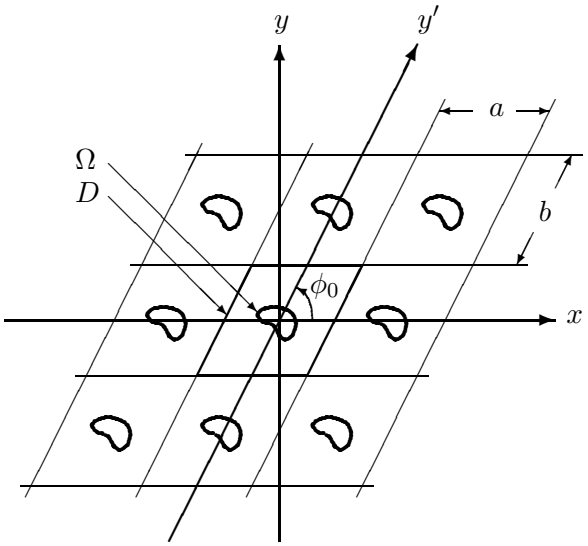

Figure 3: The periodicity of the FSS.

erties of the individual boundary or layer. For every layer a propagation matrix $\mathbf{P}^m$ is calculated. These scattering matrices are cascade coupled to form an overall scattering matrix $\mathbf{S}$ for the complete FSS, see Figure 4. This scattering matrix gives the overall transmission and reflection properties of the FSS. The mode coefficients and fields can be found at every boundary and inside every layer.

A substantial number of evanescent modes must be included in the numerical calculations. This is because the uniform sections are usually relatively short in length and thus the amplitude of the decaying modes may still be significant at the next junction. An important question is: How many Floquet modes and waveguide modes are needed? The rule of thumb is that the value of the maximum transverse wavenumber should be the same in all regions to obtain good mode matching.

The current method is implemented in MATLAB. The eigenvalue problem for the waveguide modes was solved by FEMLAB [3]. FEMLAB is a commercial FEM program, which can be integrated in MATLAB as a toolbox. Extensive discussions on the geometry and the method can be found in [12, 13].

In all examples in the paper, the incident field is a TE-polarized plane wave at normal incidence. More general polarization and direction of incidence are possible, but not shown in this paper. The power losses are calculated at the frequency with maximum transmission. In all numerical examples the metallic screen is made of copper.

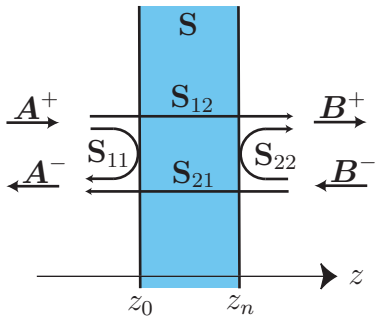

Figure 4: Scattering matrix for an FSS.

3 Scattering matrices

3.1 Scattering matrix and cascade coupling

In Figure 4, $\boldsymbol{A}^+$ and $\boldsymbol{B}^-$ are column matrices containing the mode coefficients of the total incident field. The column matrices $\boldsymbol{A}^-$ and $\boldsymbol{B}^+$ contain the mode coefficients of the total scattered field. The characteristics of the FSS are given by a scattering matrix $\mathbf{S}$,

$$\begin{pmatrix} \boldsymbol{A}^- \\ \boldsymbol{B}^+ \end{pmatrix} = \mathbf{S} \begin{pmatrix} \boldsymbol{A}^+ \\ \boldsymbol{B}^- \end{pmatrix} = \begin{pmatrix} \mathbf{S}_{11} & \mathbf{S}_{12} \\ \mathbf{S}_{21} & \mathbf{S}_{22} \end{pmatrix} \begin{pmatrix} \boldsymbol{A}^+ \\ \boldsymbol{B}^- \end{pmatrix}. \tag{3.1}$$

The elements of $\mathbf{S}$ describe the coupling between the modes on the left-hand side and the modes on the right-hand side of the FSS.

If there is no source on the right-hand side, *i.e.*, $\boldsymbol{B}^- = \mathbf{0}$, then $\boldsymbol{A}^- = \mathbf{S}_{11}\boldsymbol{A}^+$, and hence $\mathbf{S}_{11}$ is the reflection matrix. The transmission matrix of the FSS is $\mathbf{S}_{21}$ since $\boldsymbol{B}^+ = \mathbf{S}_{21}\boldsymbol{A}^+$. In this paper only reciprocal materials are considered and that implies that $\mathbf{S}_{12} = \mathbf{S}_{21}$.

By an iterative method, the scattering matrix of the complete FSS is formed from the individual scattering matrices. If two scattering matrices $\mathbf{S}^{\mathrm{a}}$ and $\mathbf{S}^{\mathrm{b}}$ are cascaded, then the matrix elements of the cascaded scattering matrix $\mathbf{S}^{\mathrm{c}}$ are given by

$$\begin{cases} \mathbf{S}^{\mathrm{c}}_{11} = \mathbf{S}^{\mathrm{a}}_{11} + \mathbf{S}^{\mathrm{a}}_{12}(\mathbf{I} - \mathbf{S}^{\mathrm{b}}_{11}\mathbf{S}^{\mathrm{a}}_{22})^{-1}\mathbf{S}^{\mathrm{b}}_{11}\mathbf{S}^{\mathrm{a}}_{21}, \\ \mathbf{S}^{\mathrm{c}}_{12} = \mathbf{S}^{\mathrm{a}}_{12}(\mathbf{I} - \mathbf{S}^{\mathrm{b}}_{11}\mathbf{S}^{\mathrm{a}}_{22})^{-1}\mathbf{S}^{\mathrm{b}}_{12}, \\ \mathbf{S}^{\mathrm{c}}_{21} = \mathbf{S}^{\mathrm{b}}_{21}(\mathbf{I} - \mathbf{S}^{\mathrm{a}}_{22}\mathbf{S}^{\mathrm{b}}_{11})^{-1}\mathbf{S}^{\mathrm{a}}_{21}, \\ \mathbf{S}^{\mathrm{c}}_{22} = \mathbf{S}^{\mathrm{b}}_{22} + \mathbf{S}^{\mathrm{b}}_{21}(\mathbf{I} - \mathbf{S}^{\mathrm{a}}_{22}\mathbf{S}^{\mathrm{b}}_{11})^{-1}\mathbf{S}^{\mathrm{a}}_{22}\mathbf{S}^{\mathrm{b}}_{12}, \end{cases} \tag{3.2}$$

where $\mathbf{I}$ is the unit matrix.

3.2 Internal fields

In order to determine the dissipation in a layer of the FSS, the mode coefficients and the fields in that layer have to be calculated. Below, the mode coefficients $\boldsymbol{C}^{\pm}$ at the boundaries $z = z_m$ and $z = z_{m+1}$ in the layer, denoted C, between these boundaries, see Figure 5, are calculated from the incident mode coefficients $\boldsymbol{A}^+$.

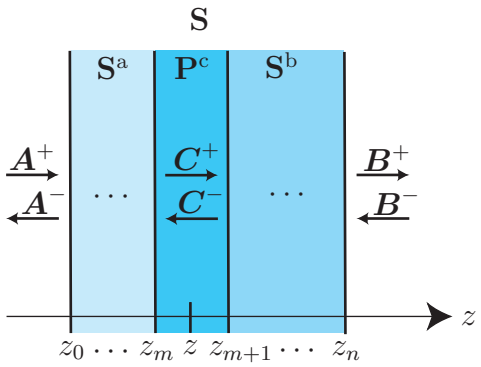

Figure 5: Inside the FSS.

Suppose there is no source on the right-hand side, *i.e.*, $\boldsymbol{B}^- = \mathbf{0}$, then

$$\begin{cases} \boldsymbol{A}^-(z_0) = \mathbf{S}_{11}\boldsymbol{A}^+(z_0), \\ \boldsymbol{B}^+(z_n) = \mathbf{S}_{21}\boldsymbol{A}^+(z_0), \end{cases} \tag{3.3}$$

If the scattering matrices $\mathbf{S}^{\mathrm{a}}$ and $\mathbf{S}^{\mathrm{b}}$ are known and the propagation matrix for the layer C is $\mathbf{P}^{\mathrm{c}}$, then

$$\begin{cases} \boldsymbol{A}^-(z_0) = \mathbf{S}^{\mathrm{a}}_{11}\boldsymbol{A}^+(z_0) + \mathbf{S}^{\mathrm{a}}_{12}\boldsymbol{C}^-(z_m), \\ \boldsymbol{C}^+(z_m) = \mathbf{S}^{\mathrm{a}}_{21}\boldsymbol{A}^+(z_0) + \mathbf{S}^{\mathrm{a}}_{22}\boldsymbol{C}^-(z_m), \end{cases} \tag{3.4}$$

$$\begin{cases} \boldsymbol{C}^-(z_{m+1}) = \mathbf{S}^{\mathrm{b}}_{11}\boldsymbol{C}^+(z_{m+1}), \\ \boldsymbol{B}^+(z_n) = \mathbf{S}^{\mathrm{b}}_{21}\boldsymbol{C}^+(z_{m+1}), \end{cases} \tag{3.5}$$

and

$$\begin{cases} \boldsymbol{C}^-(z_m) = \mathbf{P}^{\mathrm{c}}_{12}\boldsymbol{C}^-(z_{m+1}), \\ \boldsymbol{C}^+(z_{m+1}) = \mathbf{P}^{\mathrm{c}}_{21}\boldsymbol{C}^+(z_m). \end{cases} \tag{3.6}$$

From (3.4), (3.5) and (3.6), the mode coefficients $\boldsymbol{C}^{\pm}$ at $z = z_m$ are determined as

$$\begin{cases} \boldsymbol{C}^+(z_m) = (\mathbf{I} - \mathbf{S}^{\mathrm{a}}_{22}\mathbf{P}^{\mathrm{c}}_{12}\mathbf{S}^{\mathrm{b}}_{11}\mathbf{P}^{\mathrm{c}}_{21})^{-1}\mathbf{S}^{\mathrm{a}}_{21}\boldsymbol{A}^+(z_0), \\ \boldsymbol{C}^-(z_m) = \mathbf{P}^{\mathrm{c}}_{12}\mathbf{S}^{\mathrm{b}}_{11}\mathbf{P}^{\mathrm{c}}_{21}\boldsymbol{C}^+(z_m), \end{cases} \tag{3.7}$$

and at $z = z_{m+1}$ as

$$\begin{cases} \boldsymbol{C}^+(z_{m+1}) = (\mathbf{I} - \mathbf{P}^{\mathrm{c}}_{21}\mathbf{S}^{\mathrm{a}}_{22}\mathbf{P}^{\mathrm{c}}_{12}\mathbf{S}^{\mathrm{b}}_{11})^{-1}\mathbf{P}^{\mathrm{c}}_{21}\mathbf{S}^{\mathrm{a}}_{21}\boldsymbol{A}^+(z_0), \\ \boldsymbol{C}^-(z_{m+1}) = \mathbf{S}^{\mathrm{b}}_{11}\boldsymbol{C}^+(z_{m+1}). \end{cases} \tag{3.8}$$

When the FSS is processed from left to right, the scattering matrices are calculated, cascaded and saved at all layers. In this case only the scattering matrices $\mathbf{S}^{\mathrm{a}}$ and $\mathbf{S}$ are known, while $\mathbf{S}^{\mathrm{b}}$ is unknown. By utilizing (3.3)a and (3.4)a, it is seen that

$$\boldsymbol{C}^+(z_m) = (\mathbf{S}^{\mathrm{a}}_{21}(\mathbf{S}_{11} - \mathbf{S}^{\mathrm{a}}_{11})^{-1}\mathbf{S}^{\mathrm{a}}_{12} + \mathbf{S}^{\mathrm{a}}_{22})\boldsymbol{C}^-(z_m). \tag{3.9}$$

A comparison with (3.7) gives

$$\mathbf{P}_{12}^{\mathrm{c}}\mathbf{S}_{11}^{\mathrm{b}}\mathbf{P}_{21}^{\mathrm{c}} = (\mathbf{S}_{21}^{\mathrm{a}}(\mathbf{S}_{11} - \mathbf{S}_{11}^{\mathrm{a}})^{-1}\mathbf{S}_{12}^{\mathrm{a}} + \mathbf{S}_{22}^{\mathrm{a}})^{-1}. \tag{3.10}$$

In order to determine the dissipation inside a layer, the mode coefficients and the fields at that point must be calculated. Below the mode coefficients at $z \in [z_m, z_{m+1}]$ in the layer C are calculated, see Figure 5.

The mode coefficients at z are

$$\begin{cases} \boldsymbol{C}^+(z) = \mathbf{P}_{12}^{\mathrm{c}}(z - z_m)\boldsymbol{C}^+(z_m), \\ \boldsymbol{C}^-(z) = \mathbf{P}_{21}^{\mathrm{c}}(z_{m+1} - z)\boldsymbol{C}^-(z_{m+1}), \end{cases} \tag{3.11}$$

where $\mathbf{P}_{12}^{\mathrm{c}}(z - z_m)$ and $\mathbf{P}_{21}^{\mathrm{c}}(z_{m+1} - z)$ are propagation matrices from z_m to z and from z_{m+1} to z, respectively.

4 Power flow

The time-average power flow across a surface Ω in the z-direction is given by the integral of the complex Poyntings vector over that surface,

$$\begin{aligned} P &= \int_\Omega \hat{\boldsymbol{z}} \cdot < \boldsymbol{S} > \mathrm{d}a \\ &= \frac{1}{2}\,\mathrm{Re}\int_\Omega \hat{\boldsymbol{z}} \cdot \{\boldsymbol{E} \times \boldsymbol{H}^*\}\,\mathrm{d}a = \frac{1}{2}\,\mathrm{Re}\int_\Omega \hat{\boldsymbol{z}} \cdot \{\boldsymbol{E}_{\mathrm{T}} \times \boldsymbol{H}_{\mathrm{T}}^*\}\,\mathrm{d}a, \end{aligned} \tag{4.1}$$

where $*$ denotes complex conjugate, and $\boldsymbol{E}_{\mathrm{T}}, \boldsymbol{H}_{\mathrm{T}}$ are the transverse fields. The real power is given by the real part of P, while the imaginary part represents energy stored in the electric and magnetic fields.

4.1 Power flow inside the dielectric layers

The total transverse electric and magnetic fields outside the structure and inside the dielectric layers can be written as

$$\begin{cases} \boldsymbol{E}_{\mathrm{T}}^{\mathrm{d}}(\boldsymbol{r}) = \sum_{ln}\{a_{ln}^+ \mathrm{e}^{\mathrm{i}\gamma_n z} + a_{ln}^- \mathrm{e}^{-\mathrm{i}\gamma_n z}\}\boldsymbol{R}_{\mathrm{T}ln}(\boldsymbol{\rho}), \\ \boldsymbol{H}_{\mathrm{T}}^{\mathrm{d}}(\boldsymbol{r}) = \sum_{ln}\{a_{ln}^+ \mathrm{e}^{\mathrm{i}\gamma_n z} - a_{ln}^- \mathrm{e}^{-\mathrm{i}\gamma_n z}\}\boldsymbol{T}_{\mathrm{T}ln}(\boldsymbol{\rho}), \end{cases} \tag{4.2}$$

where $\boldsymbol{R}_{\mathrm{T}ln}$ and $\boldsymbol{T}_{\mathrm{T}ln}$ are Floquet modes, see [12, 13]. The relation between $\boldsymbol{R}_{\mathrm{T}ln}$ and $\boldsymbol{T}_{\mathrm{T}ln}$ is

$$\eta_0 \boldsymbol{T}_{\mathrm{T}ln} \times \hat{z} = Y_{ln}\boldsymbol{R}_{\mathrm{T}ln}, \tag{4.3}$$

where η_0 is the free space wave impedance and Y_{ln} is the mode admittance

$$Y_{ln} = \begin{cases} \frac{\gamma_n}{\mu k_0}, & l = 1, \\ \frac{\epsilon k_0}{\gamma_n}, & l = 2. \end{cases} \tag{4.4}$$

The Floquet modes are tangential plane waves, where $l = 1$ and $l = 2$ represent TE and TM polarized waves, respectively. They are orthogonal to each other in the sense that

$$\int_D \hat{\boldsymbol{z}} \cdot \{\boldsymbol{R}_{\mathrm{T}ln} \times \boldsymbol{T}^*_{\mathrm{T}l'n'}\} \,\mathrm{d}a = \frac{Y^*_{l'n'}}{\eta_0} \int_D \boldsymbol{R}_{\mathrm{T}ln} \cdot \boldsymbol{R}^*_{\mathrm{T}l'n'} \,\mathrm{d}a = \frac{Y^*_{ln}}{\eta_0} \delta_{ll'} \delta_{nn'}, \tag{4.5}$$

where D is the unit cell. Thus, the time-average power flow across the surface D in the z-direction is

$$\begin{aligned} P^{\mathrm{d}} &= \mathrm{Re} \sum_{ln} \frac{Y^*_{ln}}{2\eta_0} \{(a^+_{ln} \mathrm{e}^{\mathrm{i}\gamma_n z} + a^-_{ln} \mathrm{e}^{-\mathrm{i}\gamma_n z})(a^{+*}_{ln} \mathrm{e}^{-\mathrm{i}\gamma^*_n z} - a^{-*}_{ln} \mathrm{e}^{\mathrm{i}\gamma^*_n z})\} \\ &= \mathrm{Re} \sum_{ln} \frac{Y^*_{ln}}{2\eta_0} \{|a^+_{ln}|^2 \mathrm{e}^{-2\,\mathrm{Im}(\gamma_n) z} - |a^-_{ln}|^2 \mathrm{e}^{2\,\mathrm{Im}(\gamma_n) z} - \mathrm{i}2\,\mathrm{Im}(a^+_{ln} a^{-*}_{ln} \mathrm{e}^{\mathrm{i}2\,\mathrm{Re}(\gamma_n) z})\}. \end{aligned} \tag{4.6}$$

Suppose that the dielectric layer consists of a lossless material, *i.e.*, the permittivity ϵ and the permeability μ are real. For frequencies f above the cutoff frequency f_{cn} for the Floquet mode $\boldsymbol{R}_{\mathrm{T}ln}$, the mode is propagating, the transverse wavenumber τ_n is smaller than the wavenumber, and the longitudinal wavenumber γ_n is real, *i.e.*,

$$f > f_{cn} \quad \Leftrightarrow \quad \tau_n < k \quad \Leftrightarrow \quad \gamma_n \text{ real}. \tag{4.7}$$

The time-average power flow for the propagating Floquet modes across the surface D in the z-direction in a lossless dielectric is

$$P^{\mathrm{d}} = \sum_{\tau_n < k} \frac{Y_{ln}}{2\eta_0} \{|a^+_{ln}|^2 - |a^-_{ln}|^2\}. \tag{4.8}$$

For frequencies f below the cutoff frequency f_{cn}, the mode is evanescent, the transverse wavenumber τ_{mn} is larger than the wavenumber, and the longitudinal wavenumber γ_{mn} is imaginary, *i.e.*,

$$f < f_{cn} \quad \Leftrightarrow \quad \tau_n > k \quad \Leftrightarrow \quad \gamma_n \text{ imaginary}. \tag{4.9}$$

The time-average power flow for the evanescent Floquet modes across the surface D in the z-direction in a lossless dielectric is

$$P^{\mathrm{d}} = -\,\mathrm{Re} \sum_{\tau_n > k} \frac{Y^*_{ln}}{2\eta_0} \{\mathrm{i}2\,\mathrm{Im}(a^+_{ln} a^{-*}_{ln})\} = \frac{1}{\eta_0} \sum_{\tau_n > k} \mathrm{Im}(Y^*_{ln})\,\mathrm{Im}(a^+_{ln} a^{-*}_{ln}). \tag{4.10}$$

4.2 Power flow inside the waveguide

The total transverse electric and magnetic fields inside the waveguide are

$$\begin{cases} \boldsymbol{E}^{\mathrm{w}}_{\mathrm{T}}(\boldsymbol{r}, \omega) = \sum_{vp} \{b^+_{vp} \mathrm{e}^{\mathrm{i}k_{zp} z} + b^-_{vp} \mathrm{e}^{-\mathrm{i}k_{zp} z}\} \boldsymbol{E}_{\mathrm{T}vp}(\boldsymbol{\rho}, \omega), \\ \boldsymbol{H}^{\mathrm{w}}_{\mathrm{T}}(\boldsymbol{r}, \omega) = \sum_{vp} \{b^+_{vp} \mathrm{e}^{\mathrm{i}k_{zp} z} - b^-_{vp} \mathrm{e}^{-\mathrm{i}k_{zp} z}\} \boldsymbol{H}_{\mathrm{T}vp}(\boldsymbol{\rho}, \omega), \end{cases} \tag{4.11}$$

where $\boldsymbol{E}_{\mathrm{T}vp}$ and $\boldsymbol{H}_{\mathrm{T}vp}$ are waveguide modes, see [12, 13]. The relation between $\boldsymbol{E}_{\mathrm{T}vp}$ and $\boldsymbol{H}_{\mathrm{T}vp}$ are

$$\eta_0 \boldsymbol{H}_{\mathrm{T}vp} = Y_{vp} \hat{z} \times \boldsymbol{E}_{\mathrm{T}vp}, \tag{4.12}$$

where

$$Y_{vp} = \begin{cases} \sqrt{\frac{\epsilon}{\mu}}, & v = 0 \text{ (TEM)}, \\ \frac{k_{zn}}{\mu k_0}, & v = 1 \text{ (TE)}, \\ \frac{\epsilon k_0}{k_{zn}}, & v = 2 \text{ (TM)}, \end{cases} \tag{4.13}$$

is the admittance for the waveguide modes. The waveguide modes are a complete set, and they are orthogonal to each other in the sense that

$$\int_{\Omega} \hat{\boldsymbol{z}} \cdot \{\boldsymbol{E}_{\mathrm{T}vp} \times \boldsymbol{H}^*_{\mathrm{T}v'p'}\} \, \mathrm{d}a = \frac{Y^*_{vp}}{\eta_0} \delta_{vv'} \delta_{pp'}, \tag{4.14}$$

where Ω is the cross-section surface of the aperture. Thus, the time-average power flow through a cross-section Ω of the waveguide is

$$P^{\mathrm{w}} = \mathrm{Re} \sum_{vp} \frac{Y^*_{vp}}{2\eta_0} \{|b^+_{vp}|^2 \mathrm{e}^{-2\,\mathrm{Im}(k_{zp})z} - |b^-_{vp}|^2 \mathrm{e}^{2\,\mathrm{Im}(k_{zp})z} - \mathrm{i}2\,\mathrm{Im}(b^+_{vp} b^{-*}_{vp} \mathrm{e}^{\mathrm{i}2\,\mathrm{Re}(k_{zp})z})\}. \tag{4.15}$$

Suppose that the dielectric waveguide puck consists of a lossless material, *i.e.*, the permittivity ϵ and the permeability μ are real. For frequencies f above the cutoff frequency $f_{\mathrm{c}p}$ for the waveguide mode $\boldsymbol{E}_{\mathrm{T}vp}$, the mode is propagating, the transverse wavenumber $k_{\mathrm{t}p}$ is smaller than the wavenumber, and the longitudinal wavenumber k_{zp} is real, *i.e.*,

$$f > f_{\mathrm{c}p} \quad \Leftrightarrow \quad k_{\mathrm{t}p} < k \quad \Leftrightarrow \quad k_{zp} \text{ real}. \tag{4.16}$$

The time-average power flow for the propagating waveguide modes through the cross-section Ω of the dielectric puck is

$$P^{\mathrm{w}} = \sum_{k_{\mathrm{t}p} < k} \frac{Y_{vp}}{2\eta_0} \{|b^+_{vp}|^2 - |b^-_{vp}|^2\}. \tag{4.17}$$

For frequencies f below the cutoff frequency $f_{\mathrm{c}n}$, the mode is evanescent, the transverse wavenumber $k_{\mathrm{t}p}$ is larger than the wavenumber, and the longitudinal wavenumber k_{zp} is imaginary, *i.e.*,

$$f < f_{\mathrm{c}p} \quad \Leftrightarrow \quad k_{\mathrm{t}p} > k \quad \Leftrightarrow \quad k_{zp} \text{ imaginary}. \tag{4.18}$$

The time-average power flow for the evanescent waveguide modes through the cross-section Ω of the lossless dielectric puck is

$$P^{\mathrm{w}} = -\,\mathrm{Re} \sum_{k_{\mathrm{t}p} > k} \frac{Y^*_{vp}}{2\eta_0} \{\mathrm{i}2\,\mathrm{Im}(a^+_{vp} a^{-*}_{vp}\}. \tag{4.19}$$

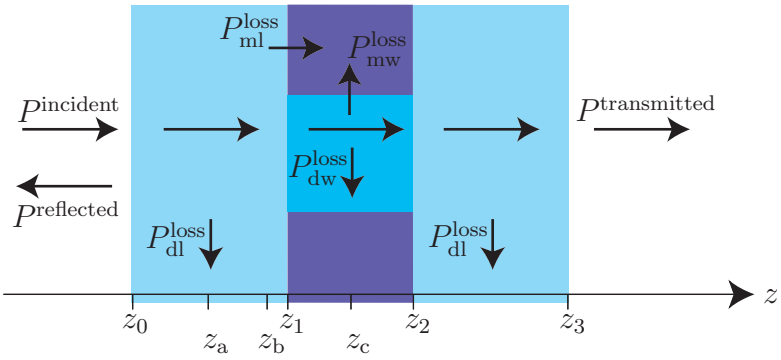

Figure 6: Power flow through an FSS.

4.3 Conservation of power

The conservation of power is satisfied, and for the FSS it yields that the incident power is equal to the sum of the reflected, transmitted, and dissipated power, see Figure 6,

$$P^{\text{incident}} = P^{\text{reflected}} + P^{\text{transmitted}} + P^{\text{dissipated}}. \tag{4.20}$$

The dissipated power is decomposed in four different parts

$$P^{\text{dissipated}} = P^{\text{loss}}_{\text{dl}} + P^{\text{loss}}_{\text{dw}} + P^{\text{loss}}_{\text{ms}} + P^{\text{loss}}_{\text{mw}}, \tag{4.21}$$

and $P^{\text{loss}}_{\text{dl}}$ is the power losses in the dielectric layers, see Section 5.1, $P^{\text{loss}}_{\text{dw}}$ is the power losses in the dielectric waveguide pucks, see Section 5.2, $P^{\text{loss}}_{\text{ms}}$ is the power losses in the plane metallic surfaces, see Section 6, and $P^{\text{loss}}_{\text{mw}}$ is the power losses in the metallic walls of the waveguides, see Section 7. The power losses can with good accuracy be determined separately. The power losses due to dissipation in the dielectric medium, $P^{\text{loss}}_{\text{dl}}$ and $P^{\text{loss}}_{\text{dw}}$, are determined under the assumption of infinite conductivity for the metallic medium, and the power losses due to finite conductivity in the metallic medium, $P^{\text{loss}}_{\text{ms}}$ and $P^{\text{loss}}_{\text{mw}}$, are determined under the assumption of lossless dielectric medium.

In this paper the dissipation is studied at frequencies with maximum transmission, *i.e.*, $P^{\text{reflected}} \approx 0$, and therefore the transmitted power is

$$P^{\text{transmitted}} \approx P^{\text{incident}} - P^{\text{dissipated}}. \tag{4.22}$$

4.4 Numerical plots of power flow through FSS

The power flow density through an FSS is illustrated in Figure 7. The structure in the two examples consists of a crossed dipole FSS and a hexagonal FSS imbedded in two dielectric layers, as in Figure 8. The incident field is a TE-polarized plane wave at normal incidence, *i.e.*, the spherical angle of incidence $\theta = 0°$, and the azimuthal angle $\phi = 0$. The contour plots of the power flow density are given at five different boundaries; at the outer boundary (between the vacuum and the dielectric layer), in the middle of the dielectric layer, in the dielectric layer 1/10 of the thickness

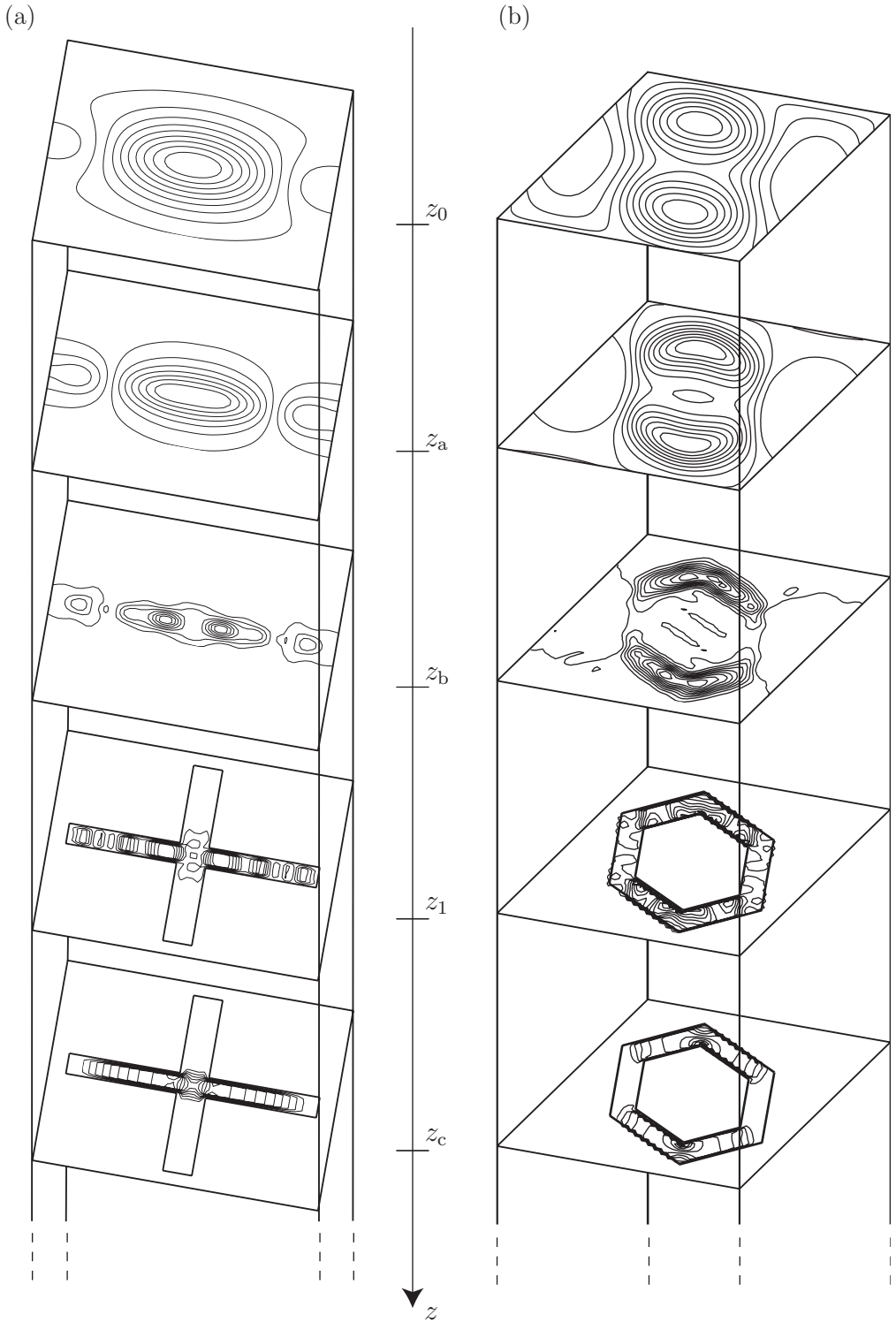

Figure 7: Power flow density for (a) a crossed dipole FSS, and (b) a hexagonal FSS, *cf.* Figure 6 and 8.

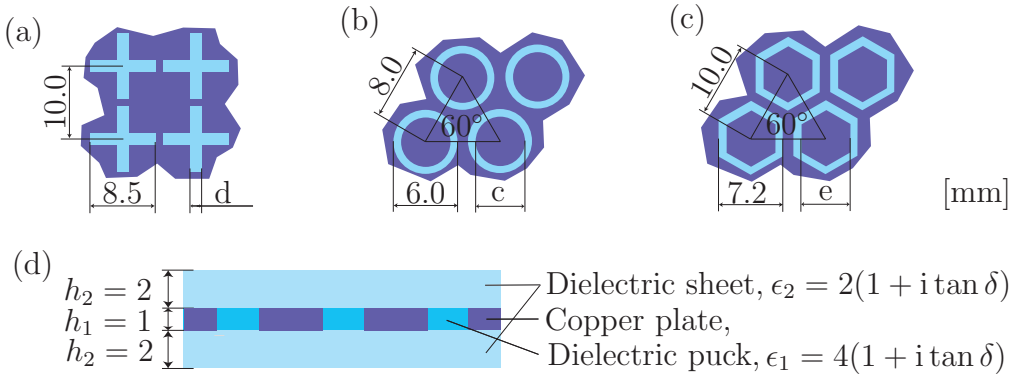

Figure 8: Three examples of FSS patterns; (a) crossed dipole FSS, (b) annular FSS, (c) hexagonal FSS. In (d) the vertical cross-section of an FSS is depicted. Cross-sections of type 1 have $d = 0.85\,\mathrm{mm}$, $c = 5.0\,\mathrm{mm}$, and $e = 5.2\,\mathrm{mm}$, while cross-sections of type 2 have $d = 1.90\,\mathrm{mm}$, $c = 4.0\,\mathrm{mm}$, and $e = 3.2\,\mathrm{mm}$.

Material	ϵ_r	ϵ_i	$\tan\delta$
Citanite	3.47	0.00750	0.0022
Plexiglas	2.59	0.00670	0.0026
Styron	2.54	0.00030	0.00012
Styramic	2.62	0.00023	0.00009
Teflon	2.08	0.00037	0.00018
Epoxy adhesive	2.80	0.056	0.020
E-glass	4.30	0.043	0.010
Rohacell 71	1.10	0.0011	0.0010

Table 1: Properties of some common dielectric materials at 10 GHz, [6].

of layer from the aperture layer, at the boundary between the dielectric layer and the aperture layer, and in the middle of the aperture layer. The power plots are symmetric around $z = z_\mathrm{c}$, this follows from invariance under time reversal for a structure that has a symmetric geometry and is non-reflecting.

5 Dielectric losses

Electric-type dissipation in the dielectric medium is modelled by the complex relative permittivity

$$\epsilon = \epsilon_\mathrm{r} + \mathrm{i}\epsilon_\mathrm{i} = \epsilon_\mathrm{r}(1 + \mathrm{i}\tan\delta), \tag{5.1}$$

where ϵ_r is the real relative dielectric constant, and $\tan\delta = \epsilon_\mathrm{i}/\epsilon_r$ is the loss tangent for the dielectric material. For a dissipative medium it is possible to introduce a conductivity σ that is related to the imaginary part of the permittivity ϵ_i as

$$\epsilon = \epsilon_\mathrm{r} + \mathrm{i}\frac{\sigma}{\omega\epsilon_0} = \epsilon_\mathrm{r} + \mathrm{i}\frac{\sigma}{2\pi f\epsilon_0}. \tag{5.2}$$

Obviously, $\tan\delta = \sigma/(2\pi f\epsilon_0\epsilon_\mathrm{r})$ is a frequency dependent function.

A "perfect dielectric" would be one for which $\tan\delta = 0$. The only perfect dielectric is vacuum. A "good dielectric" is defined to be one for which ϵ_r remains almost constant at all radio frequencies and for which $\tan\delta$ is very small. Examples of good dielectrics are polystyrene, paraffin, and teflon. There is also a group of "lossy dielectrics", characterized by a varying ϵ_r and a larger $\tan\delta$ in the radio-frequency range. Examples of lossy dielectrics are plexiglas, porcelain, and bakelite. Table 1 shows examples of complex relative permittivity for some dielectric materials at 10 GHz.

5.1 Losses in dielectric layers

The propagation in the z-direction of a Floquet mode through a lossy dielectric layer is described by, see (4.2),

$$\mathrm{e}^{\pm\mathrm{i}\gamma_n z} = \mathrm{e}^{\pm\mathrm{i}\beta_n z}\mathrm{e}^{\mp\alpha_{\mathrm{dl}n} z}, \tag{5.3}$$

where γ_n is the complex propagation constant, β_n is the phase constant, $\alpha_{\mathrm{dl}n}$ is the attenuation constant due to dissipation in the dielectric layer. The complex propagation constant can be written as

$$\begin{aligned}\gamma_n = \beta_n + \mathrm{i}\alpha_{\mathrm{dl}n} &= \sqrt{k^2 - \tau_n^2} = \sqrt{k_0^2\epsilon - \tau_n^2} = \sqrt{k_0^2\epsilon_r(1 + \mathrm{i}\tan\delta) - \tau_n^2} \\ &= \sqrt{k_0^2\epsilon_r - \tau_n^2 + \mathrm{i}k_0^2\epsilon_r\tan\delta} = \sqrt{k_0^2\epsilon_r - \tau_n^2}\sqrt{1 + \mathrm{i}\frac{k_0^2\epsilon_r}{k_0^2\epsilon_r - \tau_n^2}\tan\delta},\end{aligned} \tag{5.4}$$

where τ_n is the transverse wavenumber for the mode. When the losses are small, $\tan\delta \ll 1$, and (5.4) may be approximated by

$$\begin{aligned}\gamma_n = \beta_n + \mathrm{i}\alpha_{\mathrm{dl}n} &= \sqrt{k_0^2\epsilon_r - \tau_n^2}\left(1 + \mathrm{i}\frac{1}{2}\frac{k_0^2\epsilon_r}{k_0^2\epsilon_r - \tau_n^2}\tan\delta\right) \\ &= \sqrt{k_0^2\epsilon_r - \tau_n^2} + \mathrm{i}\frac{1}{2}\frac{k_0^2\epsilon_r}{\sqrt{k_0^2\epsilon_r - \tau_n^2}}\tan\delta.\end{aligned} \tag{5.5}$$

Hence, the phase constant and the attenuation constant are given by

$$\begin{aligned}\beta_n &= \sqrt{k_0^2\epsilon_r - \tau_n^2}, \\ \alpha_{\mathrm{dl}n} &= \frac{k_0^2\epsilon_r\tan\delta}{2\beta_n}.\end{aligned} \tag{5.6}$$

The total transmitted power $P_\mathrm{dl}^\mathrm{trans}$ through the dielectric layer can be written as

$$\begin{aligned}P_\mathrm{dl}^\mathrm{trans} = P_\mathrm{dl}^\mathrm{inc} - P_\mathrm{dl}^\mathrm{loss} &= \sum_{n=1}^{\infty} P_{\mathrm{dl}n}\mathrm{e}^{-2\alpha_{\mathrm{dl}n}\Delta z_\mathrm{dl}} \simeq \sum_{n=1}^{\infty} P_{\mathrm{dl}n}(1 - 2\alpha_{\mathrm{dl}n}\Delta z_\mathrm{dl}) \\ &= P_\mathrm{dl}^\mathrm{inc}(1 - 2\alpha_\mathrm{dl}\Delta z_\mathrm{dl}) \simeq P_\mathrm{dl}^\mathrm{inc}\mathrm{e}^{-2\alpha_\mathrm{dl}\Delta z_\mathrm{dl}},\end{aligned} \tag{5.7}$$

where $P_\mathrm{dl}^\mathrm{inc}$ is the incident power on the dielectric layer, $P_\mathrm{dl}^\mathrm{loss} \simeq P_\mathrm{dl}^\mathrm{inc} 2\alpha_\mathrm{dl}\Delta z_\mathrm{dl}$ is the total power losses in the dielectric layers, $\alpha_\mathrm{dl} = \sum_{n=1}^{\infty}\frac{P_{\mathrm{dl}n}}{P_\mathrm{dl}^\mathrm{inc}}\alpha_{\mathrm{dl}n}$ is the total attenuation constant due to dissipation in the dielectric layers, and Δz_dl is the thickness of the layers.

5.2 Dielectric losses in aperture

The propagation of a waveguide mode through an aperture with perfectly conducting walls is described by, see (4.11),

$$\mathrm{e}^{\pm \mathrm{i} k_{zp} z}. \tag{5.8}$$

The equation for the complex propagation constant $k_{zp} = \beta_p + \mathrm{i}\alpha_{\mathrm{dw}p}$ in a dielectric filled aperture becomes

$$k_{zp}^2 = (\beta_p + \mathrm{i}\alpha_{\mathrm{dw}p})^2 = k^2 - k_{tp}^2 = k_0^2 \epsilon_r (1 + \mathrm{i}\tan\delta) - k_{tp}^2, \tag{5.9}$$

where β_p is the phase constant, $\alpha_{\mathrm{dw}p}$ is the attenuation constant, and k_{tp} is the transverse wavenumber. When the losses are small, $\tan\delta \ll 1$, and for frequencies sufficiently above the cutoff frequency so that $\alpha \ll \beta$, Equation (5.9) may be approximated by

$$\beta_p^2 + \mathrm{i}2\alpha_{\mathrm{dw}p}\beta_p = k_0^2\epsilon_r - k_{tp}^2 + \mathrm{i}k_0^2\epsilon_r \tan\delta, \tag{5.10}$$

Hence

$$\begin{aligned} \beta_p^2 &= k_0^2\epsilon_r - k_{tp}^2, \\ \alpha_{\mathrm{dw}p} &= \frac{k_0^2\epsilon_r \tan\delta}{2\beta_p}, \end{aligned} \tag{5.11}$$

and the propagator of a mode is given by

$$\mathrm{e}^{\pm \mathrm{i} k_{zp} z} = \mathrm{e}^{\pm \mathrm{i}\beta_p z} \mathrm{e}^{\mp \alpha_{\mathrm{dw}p} z}, \tag{5.12}$$

where $\alpha_{\mathrm{dw}p}$ is the attenuation constant due to dissipation in the dielectric waveguide puck.

The total transmitted power $P_{\mathrm{dw}}^{\mathrm{trans}}$ through the aperture can be written as

$$P_{\mathrm{dw}}^{\mathrm{trans}} = P_{\mathrm{dw}}^{\mathrm{inc}} - P_{\mathrm{dw}}^{\mathrm{loss}} = \sum_{n=1}^{\infty} P_{\mathrm{dw}n} \mathrm{e}^{-2\alpha_{\mathrm{dw}n}\Delta z_{\mathrm{dw}}} \simeq P_{\mathrm{dw}}^{\mathrm{inc}}(1 - 2\alpha_{\mathrm{dw}}\Delta z_{\mathrm{dw}}), \tag{5.13}$$

where $P_{\mathrm{dw}}^{\mathrm{inc}}$ is the incident power in the aperture, $P_{\mathrm{dw}}^{\mathrm{loss}} \simeq P_{\mathrm{dw}}^{\mathrm{inc}} 2\alpha_{\mathrm{dw}}\Delta z_{\mathrm{dw}}$ is the total power loss in the dielectric waveguide puck, $\alpha_{\mathrm{dw}} = \sum_{n=1}^{\infty} \frac{P_{\mathrm{dw}n}}{P_{\mathrm{dw}}^{\mathrm{inc}}} \alpha_{\mathrm{dw}n}$ is the total attenuation constant due to dissipation in the dielectric waveguide puck, and Δz_{dw} is the thickness of the puck.

5.3 Numerical examples of dielectric losses

The reflected and transmitted power for a lossy structure are plotted in Figure 9. The structure consists of a lossy crossed dipole-puck aperture imbedded in two lossy dielectric layers shown in Figure 8. The complex permittivity for the puck is $\epsilon_1 = 4(1 + \mathrm{i}\tan\delta)$ and for the dielectric layer $\epsilon_2 = 2(1 + \mathrm{i}\tan\delta)$, where the loss tangent $\tan\delta = 0$, 0.001, 0.01 or 0.1. The reflected and transmitted power are plotted in three cases; losses only in the dielectric layer, losses only in the aperture layer, and losses both in the dielectric and aperture layer. The incident field is a

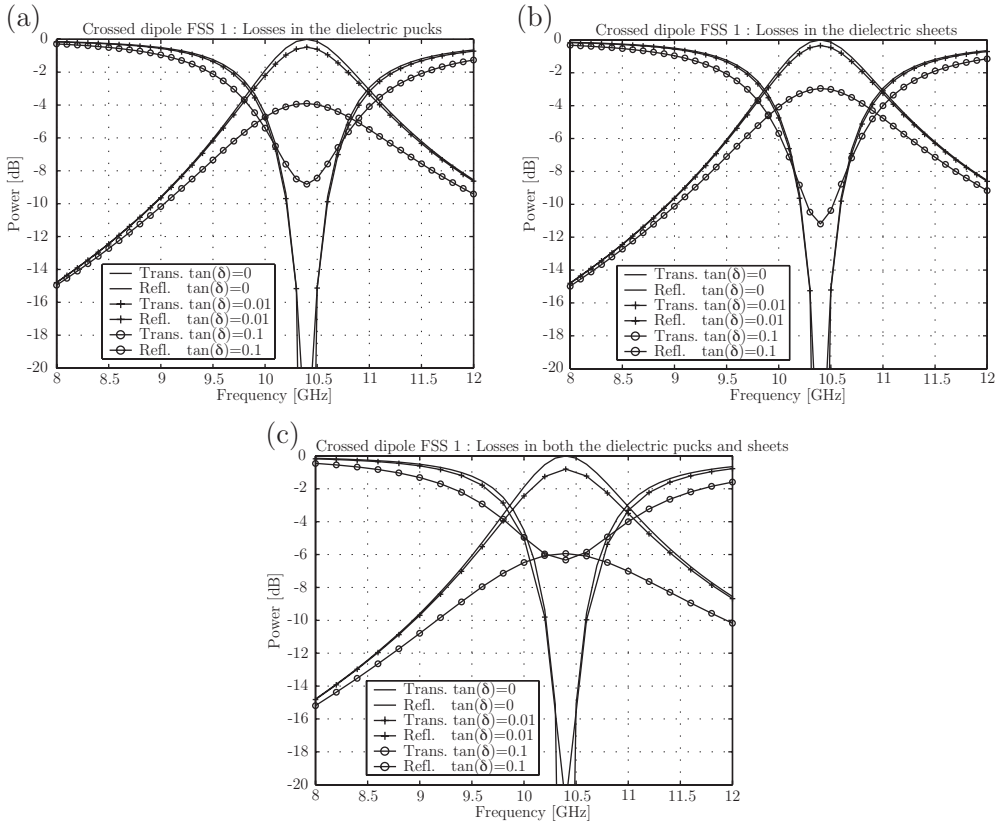

Figure 9: Dissipation in a crossed dipole FSS of type 1, *cf.* Figure 8. Both the transmitted and reflected power are plotted. The curves with a dip are the reflected power. (a) Dissipation only in the waveguide puck, (b) Dissipation only in the dielectric layers, (c) Dissipation both in the dielectric layers and the waveguide puck.

TE-polarized plane wave at normal incidence. The sharp null in the reflected power of the lossless structure does not exist when the losses are added.

Three other examples of lossy FSS are presented in Figure 10. The geometries for the FSS are shown in Figure 8. The complex permittivities for the dielectrics are the same as for the crossed dipole FSS. The reflected and transmitted power are plotted, where the loss tangent for the dielectric is the same for both the dielectric layer and the dielectric waveguide puck.

In Figure 11 a lossy structure that consists of a lossy hexagonal-puck aperture imbedded by two lossy dielectric layers is considered. The complex permittivity for the puck ϵ_1, and for the dielectric layer ϵ_2, are the same as for the crossed dipole FSS. The incident field is a TE-polarized plane wave at normal incidence.

In Table 2 numerical values of losses in the dielectric mediums are presented. Five different geometries are compared in the table; two types of crossed dipoles FSS, two types of annular FSS, and a hexagonal FSS. The cross-sections are given by Figure 8, and in the caption of that figure. The cross-sections of type 2 have

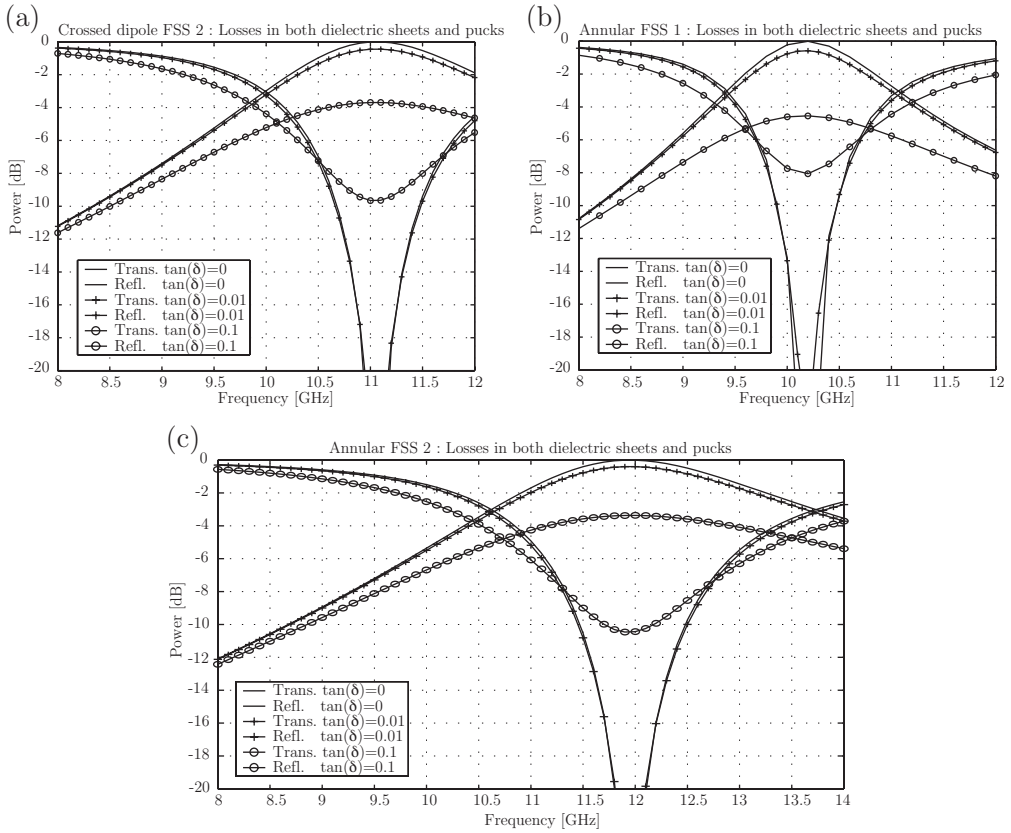

Figure 10: (a) Dissipation in a crossed dipole FSS of type 2. (b) Dissipation in an annular FSS of type 1. (c) Dissipation in an annular FSS of type 2. Both the transmitted and reflected power are plotted, where the curves with a dip are the reflected power. The geometries are given by Figure 8.

approximately twice as large apertures than cross-sections of type 1.

Numerical values of the total attenuation factors for dissipation in the dielectric are presented in Table 3. The attenuation factor due to dissipation in the dielectric layer α_{dl} and the attenuation factor due to dissipation in the dielectric waveguide puck α_{dw} are calculated for three different loss tangents, $\tan\delta = 0$, 0.001, 0.01 or 0.1. The same five structures as in Table 2 are used, see also Figure 8.

In Table 3 it can be seen that the attenuation is much larger in the dielectric waveguide puck than in the dielectric layer. This is because the fields, and therefore the power flow density, are much larger in the aperture than in the dielectric layer. The table also shows that the attenuation is smaller if the aperture is larger. This is because the power flow density is larger in a smaller aperture, and therefore the dissipation is larger in a smaller aperture.

Figure 12(a) shows the relation between the power loss and $\tan\delta$ for the hexagonal FSS (Figure 8). The three curves in the figure represent the following quantities; losses only in the dielectric layer, losses only in the waveguide puck, and losses both in the dielectric layer and waveguide puck. The corresponding attenuation factors

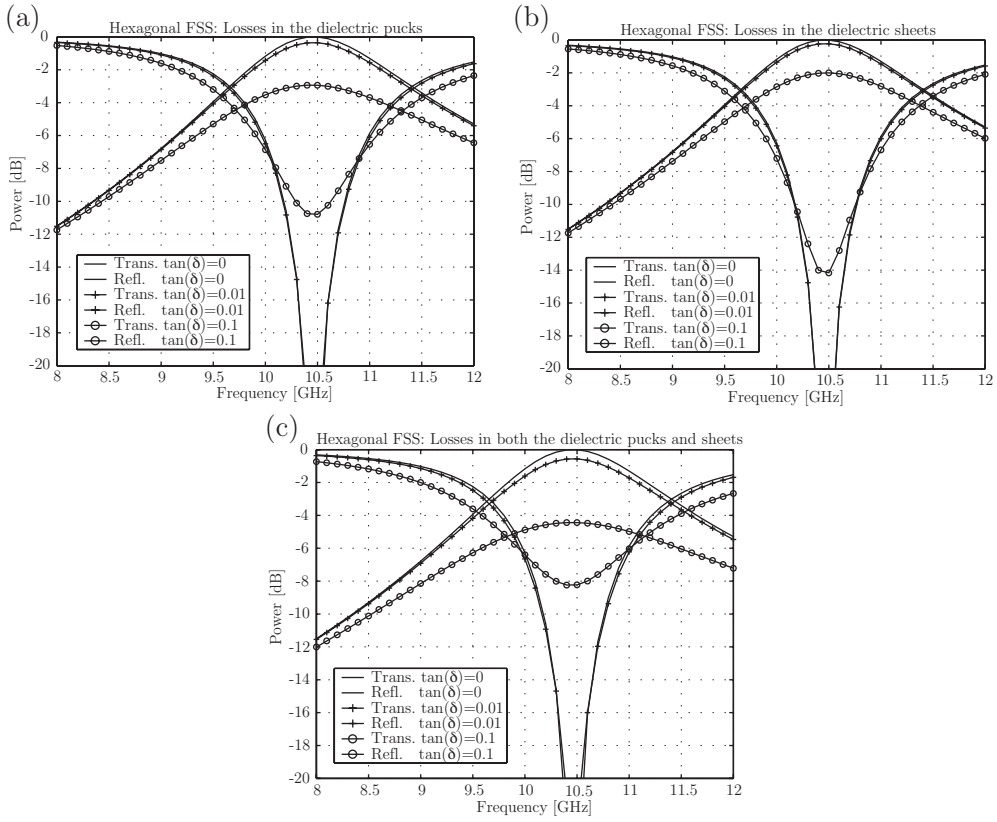

Figure 11: Dissipation in a hexagonal FSS of type 1, *cf.* Figure 8. (a) Dissipation only in the waveguide puck, (b) Dissipation only in the dielectric layers, (c) Dissipation both in the dielectric layers and the waveguide puck. Both the transmitted and reflected power are plotted, where the curves with a dip are the reflected power.

are depicted in Figure 12(b). The two curves in the figure represent the attenuation constant for dissipation in the dielectric layer and the attenuation constant for dissipation in the waveguide puck, respectively.

The total transmitted power can approximately be written as

$$P_{\mathrm{d}}^{\mathrm{trans}} = P_{\mathrm{d}}^{\mathrm{inc}} - P_{\mathrm{d}}^{\mathrm{loss}} = P_{\mathrm{d}}^{\mathrm{inc}} - (P_{\mathrm{dl}}^{\mathrm{loss}} + P_{\mathrm{dw}}^{\mathrm{loss}}) \simeq P_{\mathrm{d}}^{\mathrm{inc}}(1 - 2\alpha_{\mathrm{dl}}\Delta z_{\mathrm{dl}})(1 - 2\alpha_{\mathrm{dw}}\Delta z_{\mathrm{dw}}), \tag{5.14}$$

where $P_{\mathrm{d}}^{\mathrm{inc}}$ is the total incident power, and $P_{\mathrm{d}}^{\mathrm{loss}}$ is the total power loss due to dissipation in the dielectric mediums. The power losses in the dielectric sheets, $P_{\mathrm{dl}}^{\mathrm{loss}} = P_{\mathrm{d}}^{\mathrm{inc}} 2\alpha_{\mathrm{dl}}\Delta z_{\mathrm{dl}}$, and the power losses in the dielectric pucks, $P_{\mathrm{dw}}^{\mathrm{loss}} = P_{\mathrm{d}}^{\mathrm{inc}} 2\alpha_{\mathrm{dw}}\Delta z_{\mathrm{dw}}$, can with good approximation be determined separately. The power losses due to dissipation in the dielectric layers are determined by assuming lossless dielectric waveguide pucks, and the power losses due to dissipation in the dielectric waveguide pucks is determined by assuming lossless dielectric layers. In Tables 2 and 3, it can be seen that this is a good approximation when $\tan\delta < 0.01$.

$\tan\delta$		$P_{\mathrm{d}}^{\mathrm{loss}}$ [dB]				
Dielectric		Crossed dipole		Annular		Hexagonal
sheets	pucks	1	2	1	2	1
0	0	0	0	0	0	0
	0.001	0.049	0.022	0.046	0.026	0.035
	0.01	0.48	0.22	0.40	0.24	0.35
	0.1	3.91	1.94	3.27	2.08	2.94
0.001	0	0.035	0.023	0.025	0.019	0.023
	0.001	0.084	0.045	0.065	0.043	0.058
	0.01	0.51	0.24	0.41	0.25	0.37
	0.1	3.93	2.96	3.29	2.09	2.96
0.01	0	0.34	0.23	0.20	0.17	0.23
	0.001	0.39	0.25	0.23	0.20	0.26
	0.01	0.80	0.44	0.58	0.40	0.56
	0.1	4.13	2.13	3.41	2.21	3.10
0.1	0	2.96	2.11	1.75	1.57	2.00
	0.001	2.99	2.12	1.79	1.59	2.03
	0.01	3.31	2.28	2.08	1.76	2.28
	0.1	5.94	3.69	4.54	3.37	4.44

Table 2: Losses in the dielectric medium at the frequency with maximum transmission. The geometries are given by Figure 8.

$\tan\delta$	α_{dl} $[\mathrm{mm}^{-1}]$ α_{dw} $[\mathrm{mm}^{-1}]$				
	Crossed dipole		Annular		Hexagonal
	1	2	1	2	1
0.001	0.00100	0.00067	0.00073	0.00056	0.00066
	0.0057	0.0025	0.0053	0.0030	0.0041
0.01	0.0098	0.0066	0.0058	0.0049	0.0066
	0.055	0.025	0.046	0.028	0.040
0.1	0.085	0.061	0.050	0.045	0.058
	0.45	0.22	0.38	0.24	0.34

Table 3: Attenuation constant for dissipation in the dielectric medium. The geometries are given by Figure 8.

6 Losses in plane metallic screen

The plane metallic screen is assumed to have a finite conductivity, σ_{m}, see Figure 13, and to fulfill the condition for a good conductor, *i.e.*,

$$\sigma_{\mathrm{m}} \gg \omega\epsilon_0\epsilon_{\mathrm{m}}. \tag{6.1}$$

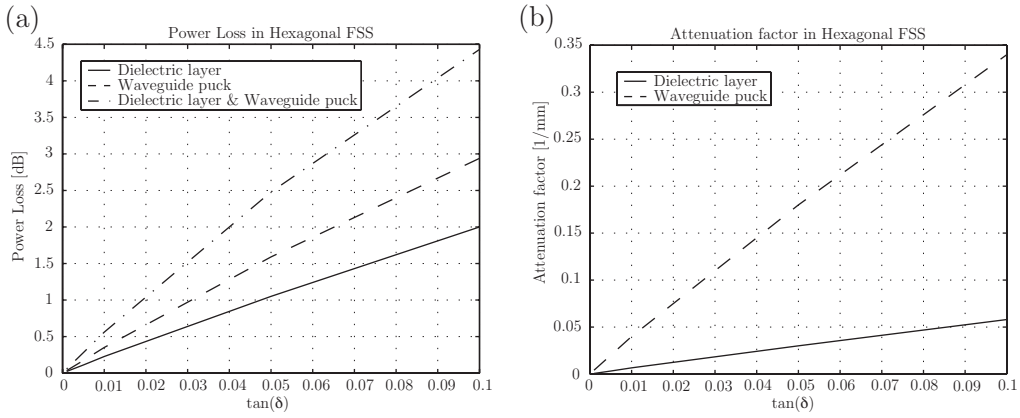

Figure 12: Power loss and attenuation constant for the hexagonal FSS. The geometry is given by Figure 8.

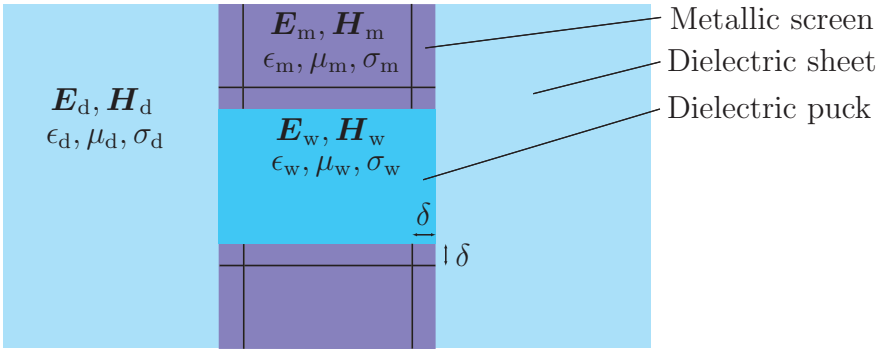

Figure 13: Skin depth, δ.

The permittivity ϵ_m and the permeability μ_m are real for the metal, and the wavenumber inside the metal is

$$k(\omega) = \frac{\omega\sqrt{\mu_\mathrm{m}}}{c_0}(\epsilon_\mathrm{m} + \mathrm{i}\frac{\sigma_\mathrm{m}}{\omega\epsilon_0})^{1/2} \approx \frac{1+\mathrm{i}}{\sqrt{2}}\sqrt{\sigma_\mathrm{m}\mu_0\mu_\mathrm{m}\omega}, \tag{6.2}$$

where (6.1) is used for the approximation.

6.1 Power losses in a plane metallic surface

Let $\hat{\xi}$ be the inward normal to the metallic surface, directed inwards the metal, see Figure 13. A plane wave propagating in the $\hat{\xi}$-direction inside the metal can be written as $\boldsymbol{E}_\mathrm{m} = \boldsymbol{E}_0 \mathrm{e}^{\mathrm{i}k\xi} = \boldsymbol{E}_0 \mathrm{e}^{\mathrm{i}\xi/\delta}\mathrm{e}^{-\xi/\delta}$, where

$$\delta = \sqrt{\frac{2}{\omega\mu_0\mu_\mathrm{m}\sigma_\mathrm{m}}} \tag{6.3}$$

is the skin depth, which is the depth for the field to decay by e^{-1}. Table 4 shows examples of conductivity and skin depth for a number of metals at 10 GHz.

Material	Conductivity, $\sigma_{\rm m}$ [S/m]	Skin depth, δ, at $f = 10$ GHz [m]	Surface resistance, $R_{\rm s}$, at $f = 10$ GHz [Ω]
Silver	$63.0 \cdot 10^6$	$0.63 \cdot 10^{-6}$	0.0125
Copper	$59.6 \cdot 10^6$	$0.65 \cdot 10^{-6}$	0.0129
Gold	$45.2 \cdot 10^6$	$0.75 \cdot 10^{-6}$	0.0148
Aluminum	$37.8 \cdot 10^6$	$0.82 \cdot 10^{-6}$	0.0162
Iron ($\mu_{\rm m} = 10^3$)	$10.4 \cdot 10^6$	$0.049 \cdot 10^{-6}$	0.0308

Table 4: Conductivity, skin depth, and surface resistance for a number of metals.

In the microwave range the skin depth is much smaller than the dimensions of the metallic screen, see Table 4. The ξ-derivatives of the fields in the metal are then much greater than the derivatives in the tangential direction. Therefore the tangential-derivatives are neglected and

$$\nabla \simeq \hat{\xi}\frac{\partial}{\partial \xi}. \tag{6.4}$$

Maxwells equations together with the assumptions (6.1) and (6.4) give that

$$\frac{\partial^2 \boldsymbol{H}_{\rm m}}{\partial \xi^2} + i\omega\mu_0\mu_{\rm m}\sigma_{\rm m}\boldsymbol{H}_{\rm m} = 0, \tag{6.5}$$

with the solution

$$\boldsymbol{H}_{\rm m} = \boldsymbol{H}_{\parallel}{\rm e}^{{\rm i}\xi/\delta}{\rm e}^{-\xi/\delta}, \tag{6.6}$$

where $\boldsymbol{H}_{\parallel}$ is the tangential component of the magnetic field at the surface of the metallic screen. A very good approximation is that the value of $\boldsymbol{H}_{\parallel}$ is the same as for a perfectly conducting screen. The corresponding electric field, which is derived from Maxwells equations, is

$$\boldsymbol{E}_{\rm m} = \frac{i-1}{\sigma_{\rm m}\delta}(\hat{\xi} \times \boldsymbol{H}_{\parallel}){\rm e}^{{\rm i}\xi/\delta}{\rm e}^{-\xi/\delta}. \tag{6.7}$$

The ohmic losses in the metal can now be calculated. The time-average of the power loss per unit volume in the metal is

$$\frac{{\rm d}P}{{\rm d}v} = \frac{1}{2}\,{\rm Re}\{\boldsymbol{J} \cdot \boldsymbol{E}_{\rm m}^*\} = \frac{\sigma_{\rm m}}{2}\boldsymbol{E}_{\rm m} \cdot \boldsymbol{E}_{\rm m}^* = \frac{1}{\sigma_{\rm m}\delta^2}|\boldsymbol{H}_{\parallel}|^2{\rm e}^{-2\xi/\delta}, \tag{6.8}$$

and the power loss density is

$$\frac{{\rm d}P}{{\rm d}a} = \int_0^\infty \frac{{\rm d}P}{{\rm d}v}\,{\rm d}\xi = \frac{1}{2\sigma_{\rm m}\delta}|\boldsymbol{H}_{\parallel}|^2 = R_{\rm s}|\boldsymbol{J}_{\rm S}|^2, \tag{6.9}$$

where $R_{\rm s} = 1/(2\sigma_{\rm m}\delta)$ is a surface resistance, *cf.* Table 4 .

The power loss on the plane metallic part of the unit cell can be written as

$$P_{\rm ms}^{\rm loss} = \frac{1}{2\sigma_{\rm m}\delta}\int_{D\setminus\Omega} |\boldsymbol{H}_{\parallel}|^2\,{\rm d}a, \tag{6.10}$$

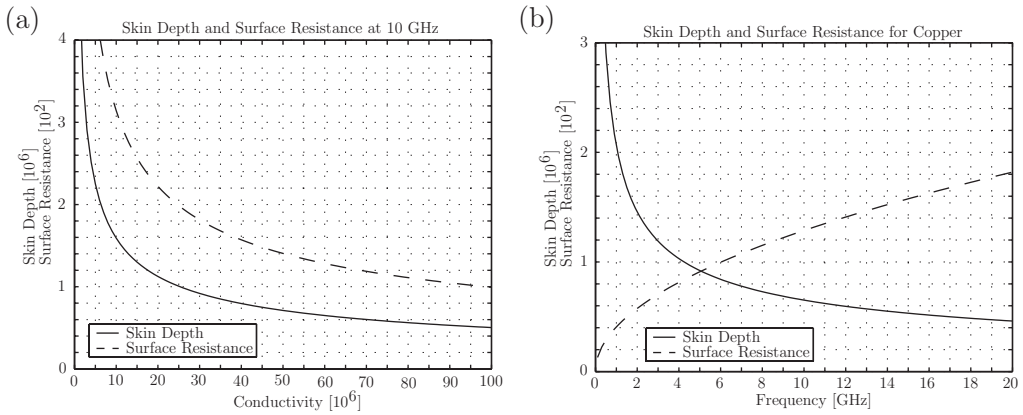

Figure 14: Skin depth, δ, and surface resistance, $R_{\rm s}$.

and the loss factor $L_{\rm f}$ due to the finite conductivity in the metallic screen is defined as

$$L_{\rm f} = \frac{P_{\rm ms}^{\rm loss}}{P_{\rm ms}^{\rm inc}}, \tag{6.11}$$

where $P_{\rm ms}^{\rm inc}$ is the incident power on the plane metallic screen.

The skin depth δ and the surface resistance $R_{\rm s}$ are depicted in Figure 14. In figure (a) the dependence of the conductivity σ at 10 GHz is plotted and in figure (b) the dependence of frequency for copper is shown.

6.2 Surface field plots and numerical examples of losses

Figures 15 and 16 are contour plots for the tangential electric and magnetic fields at the metallic surface. The fields are plotted for five different cross-sections, and for every geometry both the electric and the magnetic fields are shown; E-field to the left and H-field to the right. The incident field is a TE-polarized plane wave at normal incidence, *i.e.*, the polar angle of incidence $\theta = 0°$, and the azimuthal angle $\phi = 0°$. The electric field exists only in the aperture and is zero at the metallic surface, whereas the magnetic field exists both in the aperture and at the metallic surface.

Numerical values of the power loss $P_{\rm ms}^{\rm loss}$ at the plane metallic surface are presented in Table 5. The metallic screen is made of copper, and the power losses are calculated at both sides of the metallic plate. Five different geometries are compared in the table; two types of crossed dipoles FSS, two types of annular FSS, and a hexagonal FSS. The cross-sections are given by Figure 8, and in the caption of that figure. The cross-sections of type 2 have about twice as large apertures than the cross-sections of type 1. In Table 5 dissipation in the dielectric materials are also included. The complex permittivity for the puck is $\epsilon_1 = 4(1 + {\rm i}\tan\delta)$ and for the dielectric layer $\epsilon_2 = 2(1 + {\rm i}\tan\delta)$. The loss tangent is the same for both the puck and the layers, and four cases are studied $\tan\delta = 0$, 0.001, 0.01 or 0.1. The upper number is the power loss $P_{\rm d}^{\rm loss}$ in the dielectric mediums and the lower is the

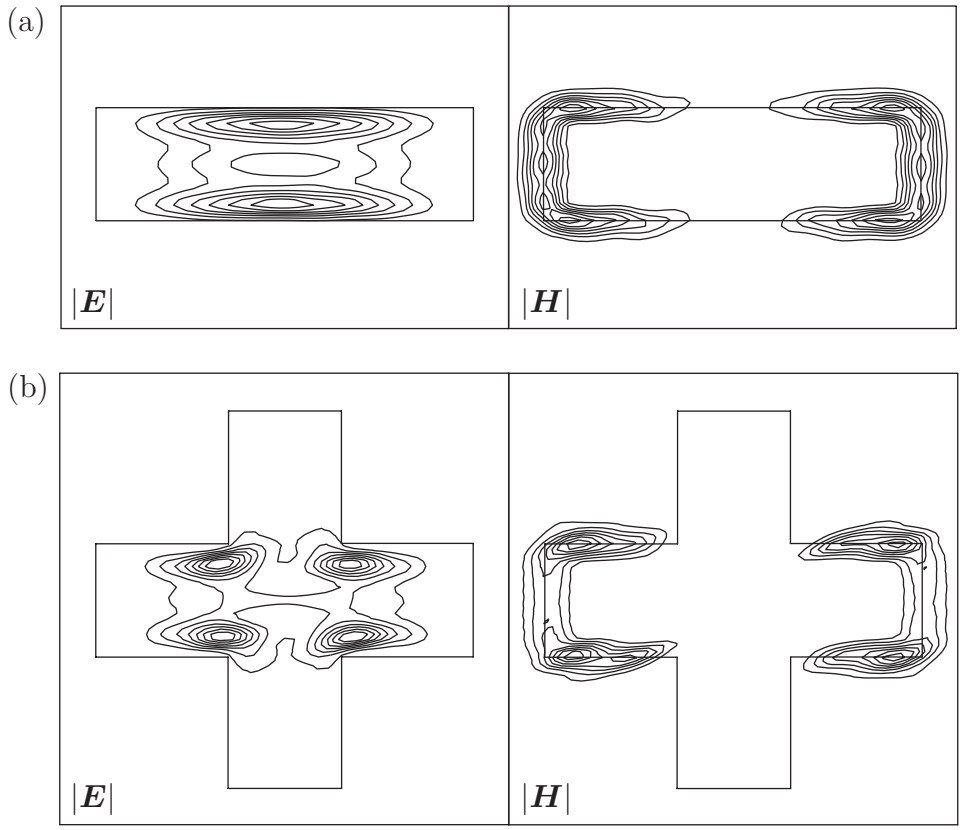

Figure 15: The electric and magnetic fields at the metallic surface; E-field on the left and H-field on the right. (a) Dipole FSS, (b) Crossed dipole FSS.

power loss $P_{\rm ms}^{\rm loss}$ in the metallic surface. The incident field is a TE-polarized plane wave at normal incidence, and the field impinges from the left side. The power loss $P_{\rm d}^{\rm loss}$ in the table indicates how much the incident field $P^{\rm inc}$ is attenuated before it reaches the metallic screen.

In Table 5 it is seen that if $\tan\delta \leq 0.001$, the power loss $P_{\rm ms}^{\rm loss}$ at the plane metallic surface is almost independent of the power loss $P_{\rm d}^{\rm loss}$ in the dielectric mediums The power loss due to finite conductivity in the plane metallic plate can therefore be determined separately, *i.e.*, the power loss $P_{\rm ms}^{\rm loss}$ is determined by assuming a lossless dielectric medium.

A comparison of the geometries of type 1 and 2 in Table 5, shows that the power loss for the plane metallic plate is much smaller for geometries of type 2. The reason is that the fields must be much larger if the aperture is smaller in order to give the same power flow P. By using $P \sim H^2 \cdot A$ and $A \sim \Gamma^2$, it can be seen that

$$P^{\rm loss} \sim H^2 \cdot \Gamma \sim \frac{\Gamma}{A} \sim \frac{1}{\sqrt{A}}, \tag{6.12}$$

where A is the area and Γ is the circumference of the aperture.

On a comparison between the losses in the dielectric medium and the plane

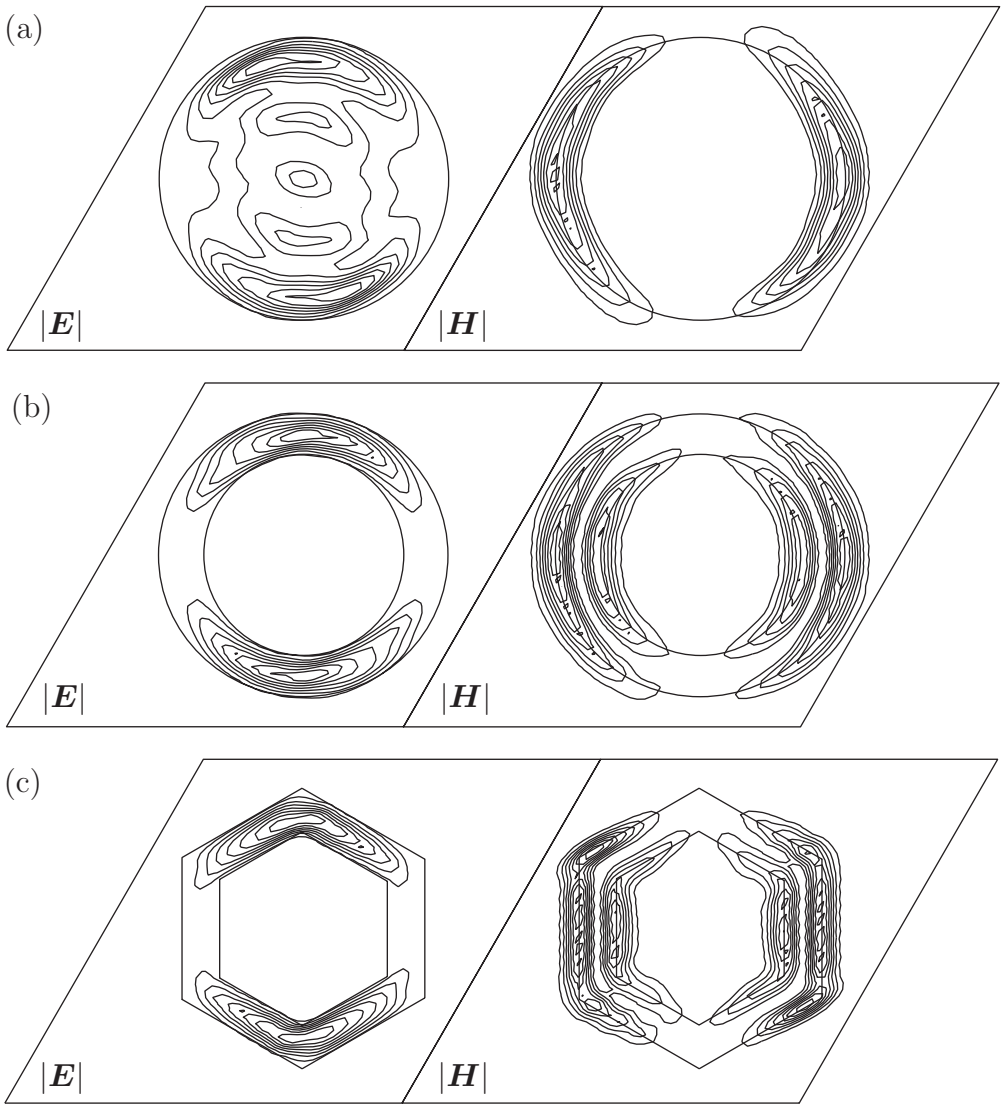

Figure 16: The electric and magnetic fields at the metallic surface; E-field on the left and H-field on the right. (a) Circular FSS, (b) Annular FSS, (c) Hexagonal FSS.

$\tan\delta$	Side	$P_{\mathrm{d}}^{\mathrm{loss}}$ [dB] $P_{\mathrm{ms}}^{\mathrm{loss}}$ [dB]				
		Crossed dipole		Annular		Hexagonal
		1	2	1	2	1
0	Left	0 0.0076	0 0.0030	0 0.0063	0 0.0030	0 0.0042
	Right	0 0.0076	0 0.0030	0 0.0063	0 0.0030	0 0.0042
0.001	Left	0.04 0.0075	0.03 0.0030	0.03 0.0062	0.03 0.0029	0.04 0.0042
	Right	0.13 0.0075	0.08 0.0030	0.11 0.0062	0.08 0.0029	0.11 0.0042
0.01	Left	0.37 0.0064	0.25 0.0028	0.22 0.0056	0.18 0.0027	0.25 0.0038
	Right	1.27 0.0063	0.66 0.0028	0.96 0.0055	0.63 0.0027	0.90 0.0037
0.1	Left	3.73 0.0026	2.35 0.0017	2.43 0.0027	1.88 0.0018	2.54 0.0020
	Right	8.92 0.0020	5.28 0.0013	7.33 0.0023	5.17 0.0014	6.88 0.0016

Table 5: The power loss $P_{\mathrm{ms}}^{\mathrm{loss}}$ at the plane metallic surface made of copper. The power losses are calculated at both sides of the metallic plate, and dissipation in the dielectric material is included with $\tan\delta$. The upper number is the power loss $P_{\mathrm{d}}^{\mathrm{loss}}$ in the dielectric medium and the lower is the power loss $P_{\mathrm{ms}}^{\mathrm{loss}}$ in the metallic surface. The geometries are given by Figure 8.

metallic plate in Table 5, it is seen that, if $\tan\delta > 0.001$ the losses in the dielectric medium are dominating.

7 Losses in waveguide walls

In the usual theory for waveguides, the walls of the waveguide are supposed to be perfectly conductive (infinite conductivity σ). In that case, a propagating waveguide mode is not attenuated in a waveguide filled with a lossless medium, and a non-propagating mode does not carry any active power. In this section the finite conductivity of the metallic walls is taken into account. It implies an attenuation of the propagating modes and also an active power transportation by the non-propagating modes.

7.1 Power losses in metallic walls

Assume that the walls of the waveguide are good, but not perfect, conductors, *i.e.*, the conductivity, σ, is large, but finite. The total electric and magnetic field inside a waveguide can be expanded in eigenmodes as [13]

$$\begin{cases} \boldsymbol{E}^{\pm}(\boldsymbol{r},\omega) = \sum_{vp} a_{vp}^{\pm}\{\boldsymbol{E}_{\mathrm{T}vp}(\boldsymbol{\rho},\omega) \pm \hat{\boldsymbol{z}} E_{zvp}(\boldsymbol{\rho})\}\mathrm{e}^{\pm \mathrm{i}k_{zp}(\omega)z}, \\ \eta_0 \boldsymbol{H}^{\pm}(\boldsymbol{r},\omega) = \sum_{p} a_{vp}^{\pm}\{\pm\eta_0 \boldsymbol{H}_{\mathrm{T}vp}(\boldsymbol{\rho},\omega) + \hat{\boldsymbol{z}} H_{zvp}(\boldsymbol{\rho})\}\mathrm{e}^{\pm \mathrm{i}k_{zp}(\omega)z}, \end{cases} \tag{7.1}$$

where $a_{vp}^{\pm}$ are expansion coefficients for the waveguide modes. From (6.9), the power loss per unit length can be written as

$$\frac{\mathrm{d}P}{\mathrm{d}z} = -\oint_{\Gamma} \frac{\mathrm{d}P}{\mathrm{d}a}\,\mathrm{d}l = -\frac{1}{2\sigma\delta}\oint_{\Gamma} |\boldsymbol{H}^{\pm}|^2\,\mathrm{d}l, \tag{7.2}$$

where Γ is the boundary of the aperture. The amplitudes of the total magnetic field at the metallic waveguide walls are

$$|\boldsymbol{H}^{\pm}|^2 = \sum_{vp} |\boldsymbol{H}_{vp}^{\pm}|^2 = \sum_{vp} |a_{vp}^{\pm}|^2\{|\boldsymbol{H}_{\mathrm{T}vp}|^2 + \frac{1}{\eta_0^2}|H_{zvp}|^2\}. \tag{7.3}$$

The total power loss in a section of length Δz_{c} of the waveguide is given by

$$P_{\mathrm{mw}}^{\mathrm{loss}} = -\frac{\mathrm{d}P}{\mathrm{d}z}\Delta z_{\mathrm{c}} = P_{\mathrm{dw}}^{\mathrm{inc}} 2\alpha_{\mathrm{c}}\Delta z_{\mathrm{c}}, \tag{7.4}$$

where $P_{\mathrm{dw}}^{\mathrm{inc}}$ is the incident power flow through the aperture, and the corresponding attenuation constant α_{c} of the field due to finite conductivity in the walls of the waveguide is

$$\begin{aligned} \alpha_{\mathrm{c}} &= -\frac{1}{2}\frac{1}{P_{\mathrm{dw}}^{\mathrm{inc}}}\frac{\mathrm{d}P}{\mathrm{d}z} = \frac{R_{\mathrm{s}}}{2}\frac{1}{P_{\mathrm{dw}}^{\mathrm{inc}}}\oint_{\Gamma} |\boldsymbol{H}^{\pm}|^2\,\mathrm{d}l \\ &= \frac{R_{\mathrm{s}}}{2}\sum_{vp}\frac{|a_{vp}^{\pm}|^2}{P_{\mathrm{dw}}^{\mathrm{inc}}}\oint_{\Gamma}\{|\boldsymbol{H}_{\mathrm{T}vp}|^2 + \frac{1}{\eta_0^2}|H_{zvp}|^2\}\,\mathrm{d}l, \end{aligned} \tag{7.5}$$

where R_{s} is the surface resistance.

7.1.1 Lossless material

Suppose that the waveguide is filled with a lossless medium, *i.e.*, the permittivity ϵ and the permeability μ are real. In a first order approximation, the modes are attenuated due to the losses in the walls, when the modes propagate through the waveguide. The frequency is above the cutoff for the mode, *i.e.*, the propagation constant k_{zp} is real. One mode that propagates in the positive z-direction is studied.

From (4.15), the time-average power flow for the mode vp in a lossless waveguide with perfectly conducting walls is

$$P_{vp}^{+} = \frac{Y_{vp}}{2\eta_0}|a_{vp}^{+}|^2, \tag{7.6}$$

where Y_{vp} is the wave impedance. Thus, the power flow with perfectly conducting walls is independent of z and the mode is not attenuated. In the case with not perfectly conducting walls, the mode looses energy when it propagates through the waveguide, due to the losses in the walls. The power P is then a decreasing function of z.

An equation for the attenuation of the power flow can be derived by combining (7.2) with (7.3) and (7.6)

$$\frac{\mathrm{d}P_{vp}^{+}}{\mathrm{d}z} = -\frac{1}{2\sigma\delta}\oint_{\Gamma}|\boldsymbol{H}_{vp}^{+}|^2\,\mathrm{d}l = -P_{vp}^{+}2\alpha_{vp}. \tag{7.7}$$

The solution to (7.7) can be written as

$$P_{vp}^{+}(z) = P_{vp}^{+}(0)\mathrm{e}^{-2\alpha_{vp}z}, \tag{7.8}$$

where $2\alpha_{vp}$ is an attenuation constant for the power

$$\alpha_{vp} = \frac{\eta_0}{2\sigma\delta Y_{vp}}\oint_{\Gamma}\{|\boldsymbol{H}_{\mathrm{T}vp}|^2 + \frac{1}{\eta_0^2}|H_{\mathrm{z}vp}|^2\}\,\mathrm{d}l. \tag{7.9}$$

This is the expression for the attenuation constant of a mode in a waveguide whose walls have good, but not perfect, conductivity.

7.2 Numerical examples of losses in aperture walls

Numerical values of the power loss $P_{\mathrm{mw}}^{\mathrm{loss}}$ in the metallic walls of the waveguide are presented in Table 6. The metallic walls are made of copper, and the power losses are calculated at the apertures on both sides of the metallic screen. Five different geometries are compared in the table; two types of crossed dipoles FSS, two types of annular FSS, and a hexagonal FSS. The cross-sections are given by Figure 8, and in the caption of that figure. The cross-sections of type 2 have about twice as large apertures than cross-sections of type 1. In Table 6 dissipation in the dielectric materials are also included. The complex permittivity for the puck is $\epsilon_1 = 4(1 + \mathrm{i}\tan\delta)$ and for the dielectric layer $\epsilon_2 = 2(1 + \mathrm{i}\tan\delta)$. The loss tangent is the same for both the puck and the layers. Four cases are studied with $\tan\delta = 0$, 0.001, 0.01 or 0.1. The power losses in the walls are calculated from the fields at the apertures on both sides of the metallic plate. The upper number is the power loss $P_{\mathrm{d}}^{\mathrm{loss}}$ in the dielectric medium and the lower is the power loss $P_{\mathrm{mw}}^{\mathrm{loss}}$ in the metallic walls. The incident field is a TE-polarized plane wave at normal incidence, and the field impinges from the left side. The power loss $P_{\mathrm{d}}^{\mathrm{loss}}$ in the table indicates how much the incident field P^{inc} is attenuated before it reaches the metallic screen.

$\tan\delta$	Aperture side	$P_{\mathrm{d}}^{\mathrm{loss}}$ [dB] $P_{\mathrm{mw}}^{\mathrm{loss}}$ [dB]				
		Crossed dipole		Annular		Hexagonal
		1	2	1	2	1
0	Left	0 0.0074	0 0.0019	0 0.0089	0 0.0028	0 0.0053
	Right	0 0.0074	0 0.0019	0 0.0089	0 0.0028	0 0.0053
0.001	Left	0.04 0.0072	0.03 0.0019	0.03 0.0088	0.03 0.0028	0.04 0.0052
	Right	0.13 0.0072	0.08 0.0019	0.11 0.0088	0.08 0.0028	0.11 0.0052
0.01	Left	0.37 0.0061	0.25 0.0018	0.22 0.0079	0.18 0.0026	0.25 0.0047
	Right	1.27 0.0061	0.66 0.0018	0.96 0.0078	0.63 0.0026	0.90 0.0047
0.1	Left	3.73 0.0020	2.35 0.0009	2.43 0.0033	1.88 0.0014	2.54 0.0020
	Right	8.92 0.0019	5.28 0.0009	7.33 0.0032	5.17 0.0013	6.88 0.0019

Table 6: The power loss $P_{\mathrm{mw}}^{\mathrm{loss}}$ in the metallic walls of the waveguide. The walls have finite conductivity and are made of copper. Dissipation in the dielectric material is included with $\tan\delta$. The power losses in the walls are calculated with help of the field at the apertures on both sides of the metallic screen. The upper number is the power loss $P_{\mathrm{d}}^{\mathrm{loss}}$ in the dielectric medium and the lower is the power loss $P_{\mathrm{mw}}^{\mathrm{loss}}$ in the metallic walls. The geometries are given by Figure 8.

In Table 6 it is seen that if $\tan\delta \leq 0.001$, the power losses $P_{\mathrm{mw}}^{\mathrm{loss}}$ in the metallic walls of the waveguide are almost independent of the loss tangent, $\tan\delta$, of the dielectric medium. The power losses due to finite conductivity in the waveguide walls can therefore be determined separately, *i.e.*, the power loss $P_{\mathrm{mw}}^{\mathrm{loss}}$ is determined by assuming a lossless dielectric medium.

When the geometries of type 1 and 2 are compared in Table 6, one sees that the power loss $P_{\mathrm{mw}}^{\mathrm{loss}}$ for the metallic walls of the waveguide is much smaller for geometries of type 2. The reason is that the fields must be much larger in a smaller aperture, in order to give the same power flow. On a comparison between the losses in the dielectric medium and the waveguide walls it is seen that, if $\tan\delta > 0.001$ the losses in the dielectric medium is dominating.

A comparison between the incident powers in Tables 5 and 6 gives that the conservation of power is fulfilled. The power that falls into the metallic layer is the same as the power that propagates through the aperture.

In Table 7 the power and the attenuation constant for the first four modes are

P_{vp} [W] & α_{vp} [mm^{-1}]					
	Crossed dipole		Annular		Hexagonal
	1	2	1	2	1
$P_{00}(0)$	—	—	0.00	0.00	0.00
α_{00}	—	—	2.20	1.20	1.24
$P_{11}(0)$	0.20	0.77	0.02	0.63	0.28
α_{11}	0.27	0.15	0.36	0.19	0.21
$P_{12}(0)$	0.79	0.22	0.98	0.37	0.72
α_{12}	0.27	0.15	0.36	0.19	0.21
$P_{13}(0)$	0.00	0.00	0.00	0.00	0.00
α_{13}	0.30	0.22	0.00	0.00	0.00

Table 7: The incident powers, P_{vp}, through the aperture and the attenuation constants, α_{vp}, for the first four modes. The geometries are given by Figure 8.

shown. The power is the incident power $P_{vp}(0)$ through the aperture, and the attenuation constant α_{vp} is due to dissipation in the walls of the waveguide, see (7.8) and (7.9). The first mode ($vp = 00$) is the TEM-mode, and other three are TE-modes ($vp = 1p$). The incident field is a TE-polarized plane wave at normal incidence. The walls of the waveguide are made of copper.

8 Conclusions

The power transmission through two examples of FSS are depicted in Figure 17. The metallic plate is made of copper and the dielectric medium has $\tan\delta = 0.001$. In figure (a) the power transmission for the annular (type 1) FSS is shown, and in (b) for the hexagonal FSS. The power decreases as it propagates through the FSS. First the power is attenuated in the dielectric sheet (1), then there is losses in the plane metallic surface (2), and after that the power is attenuated in the dielectric puck (3). The losses in the metallic waveguide walls (4) are all plotted in the middle of the waveguide, but in reality they are spread all over the walls of the waveguide.

The presence of dissipation in the dielectric mediums and on the metallic surfaces in an FSS modifies the usual description of scattering by an FSS. This modification takes the form of a complex rather than a real propagation constant, and by introduction of a surface resistance. The transmitted power is approximately given by

$$P^{\mathrm{trans}} = P^{\mathrm{inc}} t_{\mathrm{dl}} t_{\mathrm{dw}} t_{\mathrm{c}} L_{\mathrm{f}}, \tag{8.1}$$

where t_{dl} is the transmissivity due to dissipation in the dielectric layers, t_{dw} is the transmissivity due to dissipation in the dielectric waveguide puck , t_{c} is the transmissivity due to finite conductivity in the metallic walls of the waveguide, and L_{f} is the loss factor due to finite conductivity in the plane metallic surface. The transmissivities and the loss factor can with good accuracy be determined separately. The transmissivities due to dissipation in the dielectric medium, t_{dl} and t_{dw},

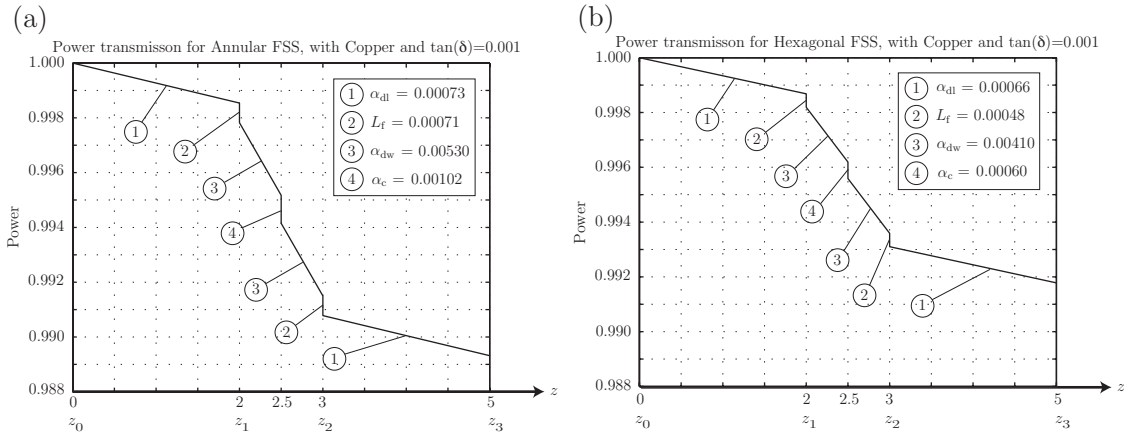

(1) Attenuation in the dielectric sheet

(2) Power losses in the plan metallic screen

(3) Attenuation in the dielectric puck

(4) Attenuation in the metallic waveguide walls

Figure 17: Power transmission through FSS, with copper plate and $\tan\delta = 0.001$ dielectric. (a) Annular FSS, (b) Hexagonal FSS. The geometries are given by Figure 8.

are determined by assuming infinite conductivity for the metallic surfaces, and the transmissivity, t_c, due to finite conductivity in the walls of the waveguide and the loss factor, L_f, due to finite conductivity in the metallic medium are determined by assuming lossless dielectric medium.

The losses in the dielectric material are rather small for common "good dielectrics", but can be quite large for "lossy dielectrics", if the thickness of the layers are large. The attenuation is proportionately larger in the dielectric waveguide puck than in the dielectric layers, if the waveguide puck and the layer have the same $\tan\delta$. This is because the fields, and therefore the power flow density, are much larger in the aperture than in the the dielectric layer. The attenuation becomes smaller if the size of the aperture becomes larger. This is because the power flow density is larger in a smaller aperture, and therefore the dissipation is larger in a smaller aperture.

The losses due to finite conductivity in the metallic plate are also rather small, if the metallic plate is made of a good conductor, such as copper or aluminium. The losses in the metallic waveguide walls are proportionately larger than the losses in the plane metallic surface. The reason is that the fields, especially the magnetic field, are larger on the waveguide walls than on the plane metallic surface. The losses on the plane metallic screen and losses on the waveguide walls are smaller, if the aperture are larger. In general, the losses in the dielectric regions are dominating over the losses due to finite conductivity in the metallic plate.

9 Acknowledgments

I would like to thank the Defense Materiel Administration in Sweden for financial support. Furthermore, I would like to thank Sören Poulsen at Celsius Applied Composites AB, ACAB, for material data and for reference data to verify the computer code.

References

[1] C. G. Christodoulou and J. F. Kauffman. On the electromagnetic scattering from infinite rectangular grids with finite conductivity. *IEEE Trans. Antennas Propagat.*, **34**(2), 144–154, February 1986.

[2] R. E. Collin. *Field Theory of Guided Waves.* IEEE Press, New York, second edition, 1991.

[3] Computer Solutions Europe AB, Stockholm. *FEMLAB: Reference Manual*, 1998.

[4] T. A. Cwik and R. Mittra. The cascade connection of planar periodic surfaces and lossy dielectric layers to form an arbitrary periodic screen. *IEEE Trans. Antennas Propagat.*, **35**(12), 1397–1405, December 1987.

[5] T. A. Cwik and R. Mittra. Correction to "The cascade connection of planar periodic surfaces and lossy dielectric layers to form an arbitrary periodic screen". *IEEE Trans. Antennas Propagat.*, **36**(9), 1335, September 1988.

[6] N. Marcuvitz. *Waveguide Handbook.* McGraw-Hill, New York, 1951.

[7] R. Mittra, T. Cwik, and C. H. Chan. Techniques for analyzing frequency selective surfaces - a review. *Proc. IEEE*, **76**(12), 1593–1615, 1988.

[8] B. Munk. *Frequency Selective Surfaces: Theory and Design.* John Wiley & Sons, New York, 2000.

[9] T. R. Schimert et al. Investigation of millimeter-wave scattering from frequency selective surfaces. *IEEE Trans. Microwave Theory Tech.*, **39**(2), 315–322, 1991.

[10] L. L. Tsai, T. K. Wu, and J. T. Mayhan. Scattering by multilayered lossy periodic strips with application to artificial dielectrics. *IEEE Trans. Antennas Propagat.*, **26**(2), 257–260, March 1978.

[11] J. C. Vardaxoglou. *Frequency Selective Surfaces (Analysis and Design).* Research Studies Press, 1997.

[12] B. Widenberg. A general mode matching technique applied to bandpass radomes. Technical Report LUTEDX/(TEAT-7098)/1–33/(2001), Lund Institute of Technology, Department of Electroscience, P.O. Box 118, S-221 00 Lund, Sweden, 2001.

[13] B. Widenberg, S. Poulsen, and A. Karlsson. Scattering from thick frequency selective screens. *J. Electro. Waves Applic.*, **14**, 1303–1328, 2000.

[14] T. K. Wu, editor. *Frequency Selective Surface and Grid Array.* John Wiley & Sons, New York, 1995.